Magnetic Imaging

Wolfgang Kuch

Freie Universität Berlin, Institut für Experimentalphysik, Arnimallee 14, 14195 Berlin, Germany
kuch@physik.fu-berlin.de

Abstract. Imaging of magnetic domains has contributed significantly to our present level of understanding of micromagnetic phenomena. A number of modern techniques is used nowadays routinely for magnetic imaging of magnetic materials and nanostructures. In this chapter, state-of-the art techniques for imaging magnetic structures are introduced, and the underlying physical phenomena are discussed. The strengths and disadvantages as well as special features of the individual techniques will be discussed in the light of their applicability and complementarity for addressing specific questions and problems.

1 Motivation

Magnetic imaging techniques allow the most direct view on magnetic properties on a microscopic scale. Magnetic domains, microscopic regions of identical magnetization direction, can be viewed in real space, and their arrangement as a function of geometric and material properties can be studied immediately in a straightforward way. The parallel improvements of magnetic imaging techniques and micromagnetic computer simulations have lead to our substantial present level of understanding of magnetism on a microscopic lengthscale.

There are numerous cases that show the importance of magnetic imaging for the investigation of magnetic thin films and nanostructures [1]. One example that should be mentioned here is the so-called spin reorientation transitions in ultrathin magnetic films. In such films the energetically preferred axis of magnetization, the easy axis, can be either within the film plane or perpendicular to it. Transitions between these two cases, the spin reorientation transitions, may occur when changing the film thickness or the temperature. Early works on spin reorientation transitions used laterally averaging techniques, and reported a loss of magnetic order within a certain temperature range right at the spin reorientation transition [2–4]. Later on, however, it was discovered by magnetic imaging that a strong tendency towards domain formation in films with out-of-plane magnetization close to the spin reorientation transition explained the observation of zero macroscopic magnetization [5–7].

Magnetic domains generally occur if a magnetic sample is confined in one or more dimensions [8]. In this case the dipolar energy includes contributions

W. Kuch: *Magnetic Imaging*, Lect. Notes Phys. **697**, 275–320 (2006)
www.springerlink.com

from the magnetostatic poles at the sample boundaries, the energy of which can be minimized by the formation of magnetic domains. The competition between this energy and the magnetic exchange energy, which tries to align neighboring magnetic spins in parallel, leads to the occurrence of characteristic magnetic domain configurations. Figure 1 gives some explanatory examples. Panels (a) and (b) show square-shaped thin film elements of different sizes. Below a certain size, the exchange energy dominates, and a single domain state is observed. At the boundaries where magnetic flux exits the sample, the right and left edges in Fig. 1 (a), magnetic poles lead to a magnetic field, which inside the sample is opposite to the magnetization. The Zeeman energy of that field, the demagnetizing field, in the sample can be avoided if a magnetic domain configuration as shown in Fig. 1 (b) is assumed. The magnetic flux is now confined inside the sample, however at the expense of exchange energy at the boundaries between domains of different magnetization direction, the domain walls. The competition between these two energy contributions, demagnetizing energy and exchange energy, defines the energetically most favorable domain configuration. In smaller elements generally the exchange energy dominates, leading to a single domain configuration (a), while in larger elements a multi-domain configuration (b) is generally more favorable. Similar flux closure domain patterns are also observed in rectangular elements (c).

As mentioned before, films with an out-of-plane easy axis of magnetization have also a tendency towards domain formation. In an infinitely extended thin film with perpendicular magnetization the magnetic flux exiting the two film surfaces leads to a demagnetizing field inside the film equal in size to the film magnetization, but opposite in sign. This demagnetizing field can be lowered by the formation of stripe domains as shown in Fig. 1 (d). A partial flux closure outside the sample at the domain boundaries between oppositely magnetized domains leads to a reduced demagnetizing energy. Because of the formation of domain walls, this happens at the expense of exchange energy and anisotropy energy. The latter is the spin–orbit related energy difference between a magnetization direction in the film plane and perpendicular to it, the driving energy contribution for the out-of-plane magnetization direction. Since in the domain walls a magnetization component in the film plane is present, its size, together with the exchange energy, defines the total energy balance. The anisotropy energy is reduced close to the spin reorientation transition, thus facilitating the occurrence of stripe domains. An example will be presented in Sect. 3.5.

In the case of small elements, i.e. when the sample extension is limited along the magnetization axis, as well as in ultrathin films with perpendicular magnetization, the magnetic flux closure occurs mainly outside the sample. If the film thickness is increased, the formation of closure domains may become favorable, as in the case of small elements (b), (c). Such a case is schematically depicted in panel (e). Closure domains at the two surfaces of the film with

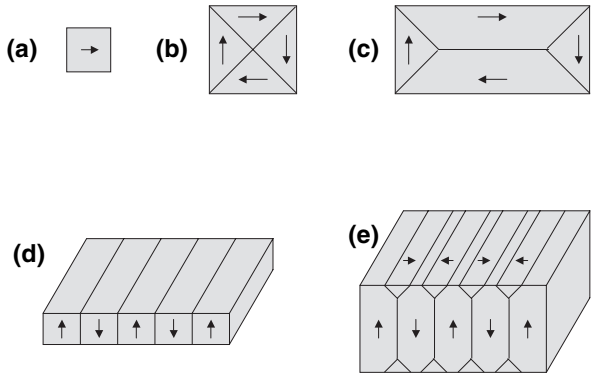

Fig. 1. Schematic explanation of occurrence of magnetic domains in different samples. (**a**): Small square magnetic element in single-domain state. Providing the demagnetization energy due to the poles at the left and right edges where magnetic flux is exiting the element and avoiding domain walls is favorable for elements below a certain size. (**b**), (**c**): In larger elements the energy needed for the creation of domain walls is provided by avoiding demagnetization energy. Closed flux domain patterns as the ones shown (Kittel, Landau pattern) avoid stray fields outside the element. (**d**): Stripe domains in a thin film sample with out-of-plane magnetization. Here the stray field outside the sample at the domain boundaries lowers the demagnetization energy in the film. This energy is balanced by the energy needed for domain wall formation. (**e**) Stripe domains in a thicker film with out-of-plane magnetization. Here the stray field outside the sample is reduced by the creation of closure domains with in-plane magnetization at the two interfaces

magnetization direction in the film plane lower the demagnetizing energy at the cost of exchange and anisotropy energy. Depending on the parameters, this configuration may be more favorable than the situation shown in panel (d). The information depth of the magnetic imaging technique used for the investigation of such samples is thus an important issue to disentangle experimentally the domain structure. The information depth of several commonly used magnetic imaging techniques together with their basic properties will be surveyed in the following section. Examples of each of these techniques will then be presented and shortly discussed along with the advantages and shortcomings in Sect. 3.

2 Overview

This section gives a short overview of the physical interactions underlying some of the most commonly used methods for magnetic characterization, and explains which of them are used for magnetic imaging. A principal distinction of the techniques can be made by the way in which depth sensitivity

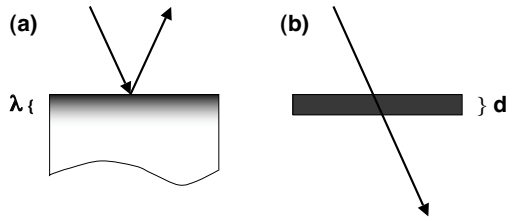

Fig. 2. Sketch of the depth information provided by on-surface (**a**) and transmission imaging methods (**b**). The surface sensitivity of the former can be characterized by the exponential information depth λ, the surface sensitivity of the latter by the maximum sample thickness d. Typically λ amounts to a few nm and d to tens of nm

is achieved. Techniques that acquire the laterally resolved magnetic information from the surface can be characterized by the information depth λ, after which the signal has decayed by a factor of $1/e$. This is schematically shown in Fig. 2 (a). The signal in the final image represents an exponentially weighted average over a certain thickness at the surface. This is represented in Fig. 2 (a) by the gradually changing graytone at the surface. Depending on the relation between sample thickness and probing depth λ, the complete depth of the sample or only the sample surface are probed. We will call techniques that work in such a way "on-surface" techniques. On-surface techniques are well suited for the investigation of very thin samples, and of samples in which the magnetic properties do not change within the sample thickness. An advantage is the insensitivity to anything that is below several times the probing depth, for example supporting layers or substrates.

A second class of magnetic imaging techniques provides information throughout the thickness of the sample, averaged with identical weighting. These are techniques in which magnetic information is gathered by a probe beam that transmits the whole sample, as sketched in Fig. 2 (b). In this case the depth sensitivity can be characterized by the upper limit on the sample thickness d for which the technique provides data within a sensible measuring time. Transmission methods are better suited for the investigation of samples in which the magnetic properties vary over the thickness (in such a case, transmission methods provide a piece of information averaged over the sample thickness in opposition to surface sensitive methods) on, or of samples that exhibit a substantial amount of non-magnetic material at the surface. A disadvantage is that the sample has to be prepared in a free-standing way, i.e., without a substrate or thick supporting layer.

Another distinction can be made by the way in which the lateral information is acquired. As generally in imaging there are two basic ways to do this, namely parallel imaging and scanning. Parallel imaging is the traditional way of image acquisition as it is used for example in optical imaging like photography etc. Parallel imaging techniques have the advantage of rapid image

creation, but pose rather high requirements on the optical elements that are used. Parallel imaging therefore often result in different image quality with respect to resolution and distortion in different positions of the image. So for example the resolution is typically higher in the center of an image than at the edges. In scanning techniques a finely focused probe beam is moved across the sample, and the image information is collected by recording a detection signal together with the information about the spatial coordinates of the probe position. The image is then reconstructed in an x-y-oscilloscope or in a computer. The image acquisition time of scanning techniques is longer compared to techniques that use parallel imaging, but the image quality is identical over the entire image, and for several techniques it is much easier to create a finely focused probe beam than to implement parallel imaging.

Magnetic imaging techniques can be further categorized by the physical interaction with the sample magnetization, just like the laterally averaging standard techniques for magnetic measurements. Table 1 lists some of the

Table 1. Commonly used physical interactions to measure integral magnetic properties and their use for magnetic imaging

Physical Interaction	Integral Method	Magnetic Imaging Method
force on electrons by $\boldsymbol{B}$ field of sample	vibrating sample magnetometry (VSM) superconducting quantum interference device (SQUID)	Lorentz microscopy
force on sample by external field	alternating gradient magnetometer (AGM)	magnetic force microscopy (MFM)
precession of magnetic moments	ferromagnetic resonance (FMR)	—
electronic properties	magneto-optical Kerr effect (MOKE)	Kerr microscopy
	x-ray magnetic circular dichroism (XMCD)	XMCD + photoelectron emission microscopy (PEEM) XMCD + transmission x-ray microscopy (M-TXM) scanning electron microscopy with polarization analysis (SEMPA) spin-polarized low energy electron microscopy (SPLEEM) spin-polarized scanning tunneling microscopy (sp-STM)

most commonly used techniques for magnetic characterization along with the underlying physical interaction. This interaction can be the Lorentz force on moving electrons by the $\boldsymbol{B}$ field of the sample, either outside or inside the sample. Standard techniques are vibrating sample magnetometry (VSM), or superconducting quantum interference devices (SQUID). In both techniques the stray field outside the sample is measured. In VSM the sample is moving, and the force on electrons in a coil is measured as induced voltage. In a SQUID also the magnetic flux outside the sample is detected by a ring that contains two Josephson contacts. One can regard this as a force on the electrons that form the supercurrent in that ring. To use the Lorentz force for magnetic imaging, it has to be detected locally at each point of the sample. A straightforward way to achieve this is to use transmission electron microscopy. This is called Lorentz microscopy and utilizes the deflection of electrons that travel through a magnetic sample by the Lorentz force of the sample's $\boldsymbol{B}$ field, inside and outside the sample, to obtain magnetic information with lateral resolution. This allows to obtain magnetic images with high resolution. We will discuss examples of Lorentz microscopy in Sect. 3.2.

A second interaction that is used for magnetic characterization is the force between the magnetic dipole of the sample and an external field. Representative for that interaction is alternating gradient magnetometry (AGM). In AGM an inhomogeneous magnetic field is created by a set of coils, and the force on the sample is measured. To enhance the detection sensitivity, the sign of the field is oscillating, and consequently also the resulting force on the sample. To implement this mechanism into an imaging technique, the force between sample and external field has to be probed locally. This is achieved by magnetic force microscopy (MFM), in which the inhomogeneous external field is generated by a sharp magnetic tip. The tip is brought into close vicinity of the sample and then scanned across the surface, while the force between sample and tip is detected. This has been successfully implemented into atomic force microscopes (AFM), which are designed to detect the small van der Waals forces between the tip and the sample surface. MFM will be discussed in Sect. 3.6.

Excitation of resonant precession of the magnetic moments in an external field by absorption of microwaves is employed during ferromagnetic resonance (FMR) measurements. There is no standard technique for magnetic imaging using local detection of FMR.

The largest number of standard techniques for magnetic imaging belongs to the class of techniques measuring magnetic properties by the corresponding electronic properties. The reason is that it is relatively easy to extend these methods used for the integral characterization of electronic properties like magneto-optical Kerr effect (MOKE) or x-ray magnetic circular dichroism (XMCD) to microscopic lateral resolution. In MOKE measurements the change in polarization of a light beam, typically from a laser, after reflection at the sample surface is detected. It is usually described within the context

of macroscopic dielectric theory. The magnetization dependent part of the polarization change after reflection can be extracted when placing the sample into an external magnetic field of varying strength and direction. XMCD measurements rely on the dependence of resonant absorption of circularly polarized soft x-rays at elemental absorption edges on the helicity of the x-rays. Here the magnetic properties of the sample enter from the spin polarization of the unoccupied part states just above the Fermi level. Both, MOKE and XMCD, can be used for magnetic imaging. Laterally resolved MOKE is termed Kerr microscopy, and will be discussed in Sect. 3.1. Lateral detection of XMCD can be achieved in various ways; here we will focus on the two most commonly used ones. Both employ already existing imaging techniques. One is photoelectron emission microscopy (PEEM). PEEM is a parallel imaging technique in which the local intensity of secondary electrons is used to create an image of the sample. After x-ray excitation, the intensity of secondary electrons is proportional to the x-ray absorption cross section, so that PEEM can be used for the laterally resolved detection of the XMCD effect. The other is transmission x-ray microscopy (TXM), in which an x-ray optics is used to obtain an image of the sample from the transmitted x-ray intensity. It is also straightforward to extend TXM for the laterally resolved detection of XMCD. We will present PEEM and magnetic TXM (M-TXM) in Sect. 3.5.

There are more magnetic imaging techniques that have to be counted to the class of techniques employing the laterally resolved detection of electronic properties. All of them have in common that already existing imaging techniques are extended to yield magnetic information. We will discuss three of them, namely scanning electron microscopy with polarization analysis (SEMPA), spin polarized low energy electron microscopy (SPLEEM), and spin-polarized scanning electron microscopy (sp-STM). SEMPA is an extension of scanning electron microscopy (SEM). In SEM a finely focused electron beam is scanned across the sample surface, and the local reflected electron intensity provides the image information. SEMPA takes advantage of the fact that secondary electrons scattered from a magnetic surface are in general spin-polarized because of the spin-polarized electronic states. Inserting a spin detector into a SEM and detecting the spin polarization of the secondary electrons as image information thus allows to obtain magnetic images. SEMPA will be discussed in Sect. 3.3.

A low energy electron microscope (LEEM) comprises an electron optics that uses elastically reflected electrons of low energy to create an image of the sample. In SPLEEM a spin-polarized electron gun is used so that the incoming electrons on the sample are spin-polarized. The reflection coefficient at low electron energies, close to the Fermi level, is strongly spin-dependent due to the spin-polarization of the unoccupied states. The final image in SPLEEM therefore contains magnetic information. SPLEEM will be presented in Sect. 3.4.

Sp-STM is technically different from the other electronic-property-based techniques since it is a scanning probe technique, similar to AFM and MFM. It relies on the dependence of the electron tunnel probability between a magnetic tip and the magnetic sample on the spin-polarized electronic states of both, tip and sample. This can be implemented into a scanning tunneling microscope (STM) by adding a magnetic tip and modulating the tunnel voltage between tip and sample, or the magnetization direction of the tip, resulting in magnetic imaging with highest lateral resolution. This will be discussed in Sect. 3.6.

3 Techniques for Magnetic Domain Imaging

In this section the techniques already listed in the previous section will be shortly presented. The sequence in which they will be presented differs from the list of Table 1 for didactic reasons. A typical example is given for each technique, and the specific features, advantages and shortcomings are discussed. The purpose of this chapter is to give an overview about a number of existing and commonly used techniques for magnetic imaging, and put the reader in a position to judge which of theses techniques is suited best for a certain problem. It is not intended as a comprehensive introduction or textbook for experimentalists who plan to use any of these techniques; for this the reader is referred to the existing specific literature.

3.1 Kerr Microscopy

Kerr microscopy is the laterally resolved measurement of the magneto-optical Kerr effect (MOKE). In macroscopic dielectric theory [9], the magnetization-dependent part of the dielectric tensor leads to a magnetization-dependent change of the light polarization after reflection at a magnetic sample. In a simplified picture this may be considered as the action of the Lorentz force on the oscillating charges in the sample that are induced by the incoming electromagnetic radiation. The emission of an electromagnetic wave by the deflected charges thus exhibits a characteristically different polarization. In general both a rotation of the polarization plane and a change in the ellipticity may occur. In a MOKE experiment this is detected as the intensity change of the reflected beam after passing a polarizing filter as a function of an applied external magnetic field [10]. To employ this effect for magnetic imaging, the imaging process has to be performed either by an optical microscope set-up that provides parallel imaging of the reflected light, or by scanning a focused incoming light spot across the sample. Both methods are applied in laboratory use, where the latter is usually termed scanning Kerr microscopy. For parallel imaging two different set-ups can be employed. For use in an ultrahigh vacuum environment the distance between the sample and the closest optical element has to be typically at least several centimeters.

In this case a set-up can be employed in which the illuminating and imaging paths are completely separated. For the imaging path a light microscope with a corresponding working distance of several centimeters has to be used, which allows to place a polarizing filter as polarization detector between sample and objective lens. Because of the large working distance resolution in this case is limited to one or even two microns. The advantage is the complete polarization analysis because there are no optical elements between sample and the polarizing filters which may influence or diminish the polarization.

To obtain magnetic Kerr microscopy images with a resolution comparable to the best optical microscopes (300–500 nm), the distance between sample and objective lens has to be very small, typically one millimeter or less. This is only possible if the sample is in air. The polarizing filters have then to be positioned behind the objective lens, which has to serve both as a condenser lens for the illuminating light and as objective lens for the reflected light. In this case the polarization may be influenced by the objective lens, which results in a loss of magnetic contrast. To enhance the magnetic contrast and to get rid of other, topographic contrast sources, usually images are digitally compared to a reference image which can be taken at the same spot if the sample is magnetically saturated, for example by a high external field. Compared to other magnetic imaging techniques in this chapter the resolution of Kerr microscopy is quite moderate. In the case of parallel imaging the acquisition time for an image is rather short. Depth information is obtained in an on-surface way, with a probing depth of the order of some tens of nanometers.

An example is shown in Fig. 3. It presents magnetic domains in strained FeCoSiB amorphous ribbons [11]. Depending on the stress, different magnetic domain patterns are observed. One notices that the field of view is several hundreds of microns. This is typical for Kerr microscopy with its moderate lateral resolution, but it may be regarded as a special feature that it is quite easy to zoom out and obtain images with a large field of view. Another advantage is that the method is purely optical, and therefore can be applied in arbitrarily high external magnetic fields.

In layered systems of ultrathin films light reflection is influenced by the interference of reflected waves from the separate interfaces between the different layers. It has been shown recently that this can be used for achieving a depth selectivity by phase adjustment [12]. In this way contributions to the Kerr signal from certain depths in a multilayered sample can be enhanced or cancelled, leading to images that represent the magnetic domain pattern at different depths or of different layers [12]. Since nearly all of the most exciting new discoveries in thin-film magnetism are observed in multilayered structures in which two or more magnetic layers have to be switched separately, a magnetic imaging technique that is able to address the different magnetic layers is a substantial advantage for the microscopic investigation of such structures. With Kerr microscopy this is, within certain limits, possible.

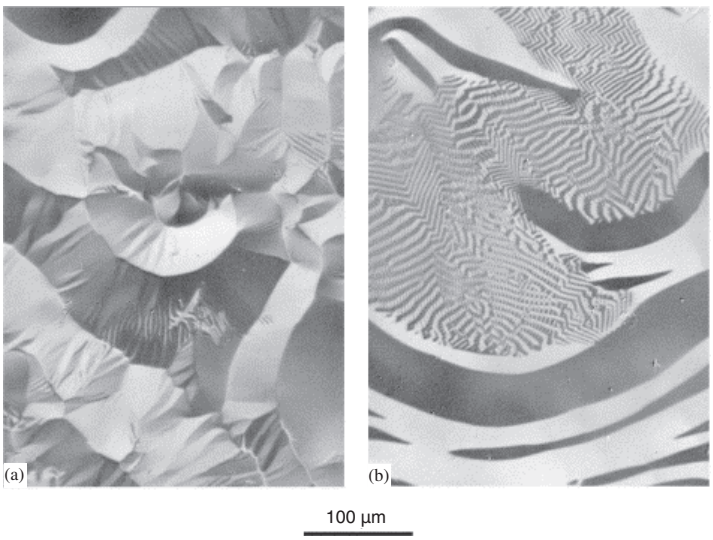

Fig. 3. Example of Kerr microscopy. Shown are magnetic domain images of FeCoSiB amorphous ribbons that exhibit a stress-induced change in domain patterns. (Reproduced from [11] with permission, copyright (2000) by Elsevier Science)

The details of how to access the magnetic information of the different magnetic layers, however, depend on the particular sample under study and have to be optimized again for each new structure.

3.2 Lorentz Microscopy

In Lorentz microscopy the force exerted by the magnetic flux density $\boldsymbol{B}$ on moving charges is used for magnetic imaging. It can be implemented without too much effort in commercial transmission electron microscopes [13,14]. The force $\boldsymbol{F}$ on a moving electron with velocity $\boldsymbol{v}$ is given by

$$\boldsymbol{F} = |e|(\boldsymbol{v} \times \boldsymbol{B}) \,, \tag{1}$$

where e is the electron charge. This force can lead to a deflection in the propagation direction of the electron if the integrated flux density, inside and outside the sample, along the electron path does not vanish. This is depicted schematically in Fig. 4. Panel (a) shows the situation in which stripe domains with in-plane magnetization are separated by domain walls aligned with the magnetization direction. In this case there is no magnetic flux outside the sample. Electrons that are transmitted through the sample experience a Lorentz force according to (1), which at domains of opposite magnetization direction points into opposite directions. The propagation paths of electrons after transmission through the sample are bent into different directions, depending on the local magnetization direction.

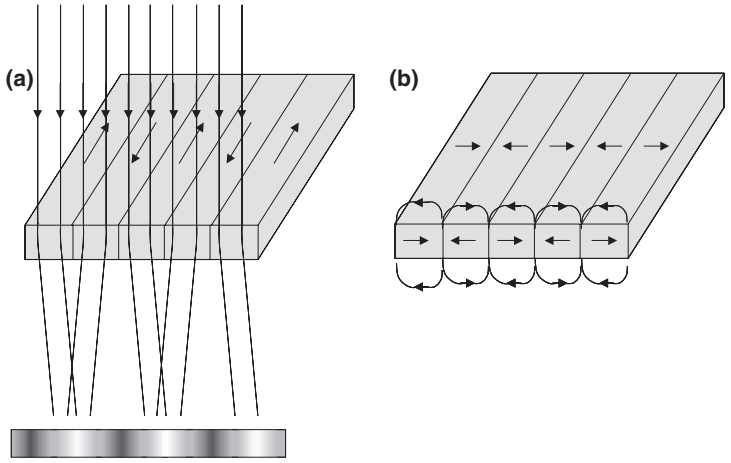

Fig. 4. Schematic explanation of Lorentz microscopy. Electrons that transmit the sample are deflected by the Lorentz force from the $\boldsymbol{B}$ field inside and outside the sample. (**a**) Situation in which 180° domains are separated by domain walls running along the magnetization axis. The $\boldsymbol{B}$ field is confined to the interior of the sample. The deflection of the electrons after transmission through the sample leads to an intensity modulation in out-of-focus images as shown schematically at the bottom. (**b**) Situation in which 180° domains are separated by domain walls running perpendicular to the magnetization axis. In this case the $\boldsymbol{B}$ field lines are closed by the stray field outside the sample. Electrons transmitted through the sample do not experience a net deflection, since the contributions from the interior of the sample and the stray fields in front and behind the sample cancel out

The situation in panel (b) is different. If stripe domains with in-plane magnetization are separated by domain walls running perpendicular to the magnetization direction, as in panel (b), the lines of the magnetic flux density are closed above and below the sample. Electrons that are transmitted through that sample do not experience a net deflection, since the contributions from the Lorentz forces inside and outside (above and below) the sample cancel out.

To implement Lorentz force contrast for magnetic imaging into a transmission electron microscope one has to recall some basic facts of optical imaging. If an ideal lens is used to image an object, all parallel rays emanating from the specimen meet in the focal plane behind the lens, located at the focal length from the optical center of the lens. In other words, all rays that are emitted at the specimen under identical angle pass the focal plane at identical position. Different emission angles, on the other hand, are represented by different positions in the focal plane. A reciprocal space image is thus present at the focal plane. The image plane, on the other hand, is defined as the plane where all rays coming from the same spot of the specimen, irrespective of the emission angle, meet again. This is where a focused real space image of the

specimen is present. The consequence for Lorentz magnetic imaging is that a deflection of the electron beam at the sample, like in Fig. 4 (a), is irrelevant for the focused image acquired in the image plane. To obtain a magnetic contrast it is therefore necessary to defocus the image. The intensity distribution of an underfocussed or overfocussed image contains a mixture of real space and angular information. As shown schematically in Fig. 4, the defocused image of the sample of panel (a) would lead to an intensity enhancement or an intensity reduction at the domain boundaries. In analogy to the light optical counterpart, in which the deflection of light in a specimen of varying optical thickness is made visible in a defocused image, this mode of operation of Lorentz microscopy is called Fresnel mode. The contrast of the actual domains in this mode is the same everywhere, but the domain walls appear with a dark or bright contrast, depending on the orientation of the domain wall with respect to the magnetization directions of the adjacent domains.

In another mode of operation part of the beam in the focal plane of the objective lens is blocked or obscured by an aperture. This selectively removes electrons from the final image according to their starting angle at the sample. Domains that lead to a deflection of passing electrons in the direction which is blocked in the focal plane consequently appear darker in the real space image taken at the image plane. By moving the aperture to block different positions according to different directions of electron deflection, the contrast of the various domains can be varied, and statements about the magnetization directions can be made.

Figure 5 shows a typical example of Lorentz microscopy from [15]. Lorentz microscopy images of two different permalloy microstructures of 2.5 µm overall length are presented. The top row, panels (a) and (b), are examples for the Fresnel mode of operation, while panels (c) and (d) show images taken in the Foucault mode of operation. It is nicely seen that in the Fresnel images (a) and (b) black and white lines are present that mark the borders between domains of different magnetization direction. For the interpretation of such images it is sometimes, in particular in the more complicated patterns as in the elements shown in Fig. 5, necessary to simulate the Fresnel image numerically and optimize the input domain configuration until agreement with the experimentally observed image is achieved. The bottom row of images in [15], panels (c) and (d), shows Foucault images of the same elements. Note that, although panels (a) and (c), as well as (b) and (d) show the same microstructures, they were imaged at different external magnetic fields and after different external field history, so that the magnetic configuration is not the same. All images were taken during application of an external field prior to switching. For details see [15]. The difference between the Fresnel and Foucault modes of operation is immediately recognized. In the Foucault images (c) and (d) the different grayscale contrasts can be directly related to the different deflection angles the electrons have acquired by the Lorentz force during their passage through the sample, provided the exact position

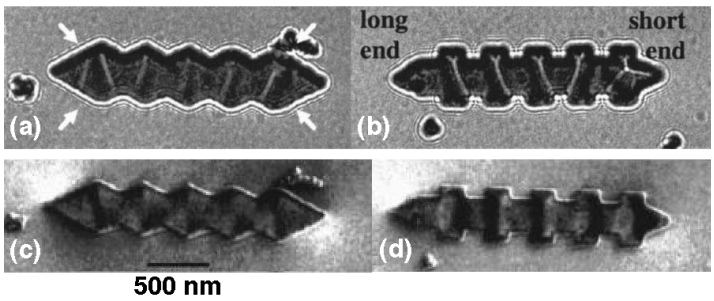

Fig. 5. Example of magnetic domain imaging by Lorentz microscopy. Shown are magnetic images of two different permalloy microstructures during reversal by an applied external magnetic field. (**a**), (**b**): Images obtained using the Fresnel mode, (**c**), (**d**): images obtained in Foucault mode (Reproduced from [15] with permission, copyright (2000) by the American Institute of Physics)

of the aperture in the focal plane with respect to the sample orientation is known. However, as already mentioned, also the stray field outside the sample contributes to this deflection. This can be nicely seen in panels (c) and (d) from the dark and white contrast at some of the edges outside the magnetic structure. At these edges stray magnetic flux is coming out of the sample. It may be regarded as an advantage of Lorentz microscopy that the stray field outside magnetic micro- and nanostructures can be imaged. For the design of structures with desired magnetic reversal properties it can be useful to know how much stray field is present at which edge of the sample. To know the stray field outside the sample also helps with the interpretation of the magnetic configuration. It has always to be kept in mind, however, that the stray field above and below the microstructures contributes to the image in an identical way, but is more difficult to separate from the actual domain structure of the element.

Instead of the two modes of operation described above, which can be implemented rather easily into transmission electron microscopes, another way of Foucault imaging is being followed with more specifically dedicated instruments. In a scanning transmission electron microscope four or more electron detectors can be positioned off-axis in the back focal plane of the objective lens in order to detect electrons passing that plane with a certain offset from the optical axis, corresponding to electrons that have experienced a deflection into a certain direction [16,17]. In this scanning mode of operation the difference between pairs of oppositely placed detectors can be used as deflection signal along one certain axis. It is then not necessary to have any detector in the image plane, since the imaging process is realized by scanning the electron beam across the sample. This mode of Lorentz microscopy is referred to as differential phase contrast microscopy.

The main advantage of Lorentz microscopy is the quite high resolution, which can be also judged from the scale of the images of Fig. 5. It can be used to study the details in switching of small magnetic structures. It is only possible to perform Lorentz microscopy in transmission. The information about the local magnetization direction is indirect, and comes from the integrated magnetic flux density along the electron trajectory. If coils are integrated into the sample holder, the technique tolerates some additional in-plane fields. However, when studying the magnetic reversal or switching of magnetic microstructures under an external field, it has to be kept in mind that usually there is a quite high perpendicular field at the sample position from the magnetic lens of the electron microscope. Lorentz microscopy is not element-selective, and there is no means to obtain depth-selective information.

3.3 Scanning Electron Microscopy with Polarization Analysis (SEMPA)

While in the last section a technique for magnetic imaging that used a transmission electron microscope has been presented, this section will deal with a technique using the column of a scanning electron microscope. It takes advantage of the fact that secondary electrons that are emitted after the absorption and inelastic scattering of a primary electron in a magnetic sample are usually spin-polarized along the spin direction of the majority electrons. Scanning the primary electron beam across the sample and detecting the spin of the secondary electrons instead of their bare intensity, as it is done in standard scanning electron microscopy, should thus yield magnetic contrast with the same high resolution as scanning electron microscopy. The difficulty is to obtain reasonable statistics in the final image. The signal of a spin detector is typically orders of magnitude lower compared to the total electron intensity, and the resolution of an electron microscope column scales inversely with the square root of the beam current.

Figure 6 sketches the set-up of scanning electron microscopy with polarization analysis (SEMPA, sometimes also termed spin-SEM). The electron beam from the microscope column hits the sample under a certain angle from the surface normal, and the emitted secondary electrons are collected by an electron optics and transferred to a spin detector [18, 19]. A spin detector usually employs the right–left asymmetry caused by the spin–orbit interaction during the scattering of electrons at high Z materials. In a Mott type detector electrons are scattered at a gold foil at rather high kinetic energies, typically 50–100 keV, while in a LEED type detector Bragg scattering at a certain optimum energy (104.6 eV) at a tungsten single crystal surface is used. The performance of a spin detector is characterized by its figure of merit, a number giving the factor by which the acquisition time has to be extended for spin detection compared to direct electron detection without spin analysis in order to reach the same counting statistics. It is given by the

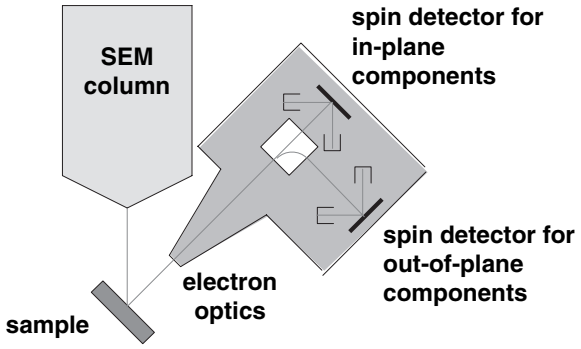

Fig. 6. Schematics of magnetic imaging by scanning electron microscopy with polarization analysis (SEMPA). A finely focussed electron beam from a scanning electron microscope column is scanned across the sample surface, and the emitted secondary electrons are transferred to a spin detector by an electron optics

square of the spin detection efficiency of the spin detector times the reduction in intensity by the spin detection with respect to the incoming signal. Typical numbers are 0.25 for the spin detection efficiency, and 1/1000 for the intensity attenuation, so that figures of merit are typically of the order of 10^{-4}. This illustrates that it is not straightforward to implement magnetic imaging by SEMPA into a standard commercial scanning electron microscope. There are special requirements to the illuminating column with respect to electron current and resolution, which can be met only with state-of-the-art field emission cathodes. The first publication of magnetic imaging with SEMPA appeared only about 20 years ago [20].

A spin detector is sensitive to the two transverse spin components of the electrons as they enter the detector. In the sketch of Fig. 6 a set-up with two spin detectors is shown. While the spin detector positioned along the surface normal is sensitive to the two in-plane components of magnetization, a second spin detector oriented at 90° delivers information about the out-of-plane component and one in-plane component. Both spin detectors can be alternatively operated by switching on and off an electrostatic electron beam deflector as depicted as a white square. The quasi-simultaneous detection of all three spin components, or in other words of all three magnetization components in the images, is one of the specific strengths of the technique. Since all the imaging process is done by the primary electron beam with a relatively high kinetic energy, all the adjustment of the electron transfer optics and the spin detectors does only influence the contrast, not the position on the image. It is therefore possible to numerically compare images that have been acquired at the same sample position but for different components of magnetization, and calculate, for example, an image of the angle of magnetization. This is one of the specific strengths of SEMPA, which is probably the only method where magnetic images for different magnetization components,

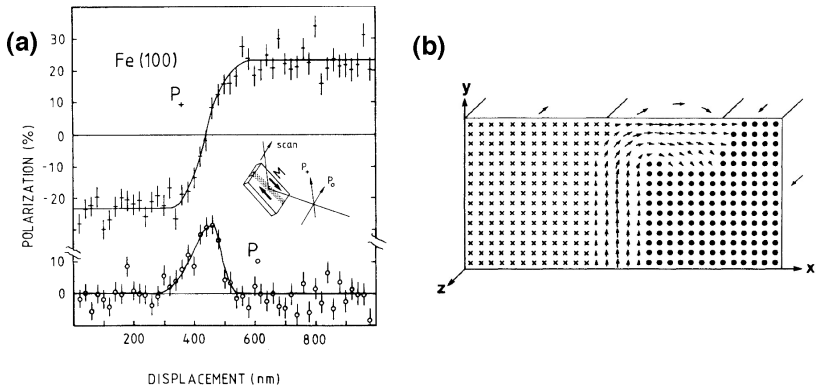

Fig. 7. Example of SEMPA. (**a**): A line scan of the two in-plane components of spin polarization across a Bloch wall of an Fe(001) single crystal reveals that the magnetization direction in the wall at the surface is rotated into the surface plane. (Reproduced from [21] with permission, copyright (1989) by the American Physical Society).) (**b**): Result of micromagnetic simulation demonstrating the magnetization configuration of such a Néel cap of a Bloch wall at the surface. (Reproduced from [22] with permission, copyright (1989) by the American Physical Society))

but with fully identical spatial information can be obtained. SEMPA images in literature are therefore often found color-coded, with colors corresponding to the two-dimensional information about the local magnetization direction, the so-called color wheel.

A famous early example of magnetic imaging by SEMPA, in which the simultaneous sensitivity to different magnetization components was used, is shown in Fig. 7. SEMPA measurements at domain walls of an Fe single crystal revealed that the magnetization direction in the wall at the surface is different from the volume of the sample [21, 22]. Figure 7 (a) shows line profiles of two components of the spin polarization across a domain wall separating two domains of opposite magnetization in Fe(001), as sketched in the inset. The upper curve, labelled P_+, represents the magnetization component along the magnetization of the adjacent domains, and consequently changes sign across the domain boundary. The lower curve, labelled P_0, represents the polarization of the spin component in the surface plane perpendicular to the magnetization of the domains. It shows the presence of a magnetization direction within the film plane inside the domain wall. This means that the magnetization rotates within the surface plane between one domain and the next. This is somewhat surprising if one considers the higher magnetostatic dipolar energy connected to the stray field of such a domain wall structure compared to the energetically more favorable configuration in which the magnetization rotates within the plane of the domain wall, a so-called Bloch wall. Figure 7 (b) shows a micromagnetic simulation. It represents a cross section through the near-surface region of a 180° domain wall. Crosses and full circles

correspond to the magnetization directions of the two domains, pointing into and out of the drawing plane, respectively. It is nicely seen how at the surface the spin structure of the domain wall changes significantly. The magnetization direction inside the wall changes from the direction perpendicular to the surface into the surface, and the wall becomes wider. The reason is to avoid magnetic poles at the surface by creating magnetic poles at the edges of the domain wall. The energy balance between these two configurations determines the actual three-dimensional spin structure of the domain wall, as displayed in Fig. 7 (b). In analogy to the so-called Néel wall of ultrathin films such a structure was termed "Néel cap" because of the similar surface spin structure.

This example demonstrates another feature of SEMPA, namely its high surface sensitivity. The attenuation length of secondary electrons is relatively short, about 2 nm; in addition, secondary electrons are created in overlayers, and the spin polarization of passing electrons is influenced by additional scattering in an overlayer. All together the information contained in a SEMPA image stems from the topmost layers in a sample. This means that surface preparation under ultrahigh vacuum conditions is necessary. Often surfaces for SEMPA imaging are prepared by depositing an ultrathin overlayer of a material with a high spin polarization, mostly iron. It is then assumed that, because of the extremely small thickness of this surface layer, the magnetic properties of the sample are not significantly affected.

The high surface sensitivity of SEMPA can be an advantage in certain cases. This is demonstrated in the next example, in which the surface of the layered antiferromagnet $La_{1.4}Sr_{1.6}Mn_2O_7$ is imaged. The left image of Fig. 8 shows the surface topography of the single crystal sample. Steps corresponding to the height of one unit cell, about 1 nm, are recognized as thin white

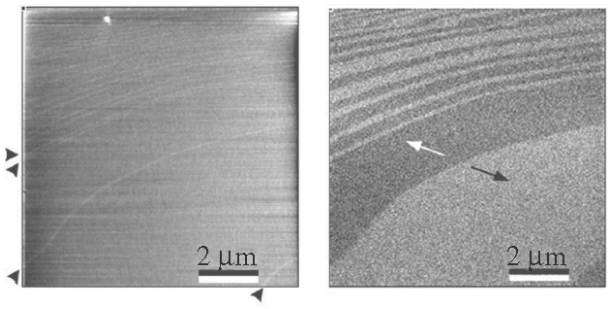

Fig. 8. Example demonstrating the surface sensitivity of SEMPA. *Left*: SEM image of the surface topography of a $La_{1.4}Sr_{1.6}Mn_2O_7$ single crystal. *Right*: Magnetic SEMPA image of the same position of the sample. The alternating grayscale contrast reflects the layered antiferromagnetic spin structure of the sample (Reproduced from [23] with permission, copyright (2004) by the American Physical Society)

lines in the scanning electron microscopy image. The right panel is the magnetic image. It is clearly seen how the spin polarization contrast reverses its sign at every terrace. The different grayscales in this image therefore reflect the opposite spin directions of the topmost layer of the sample, characteristic for such a layered antiferromagnet. This is only possible using an imaging method with a high surface sensitivity. It should be mentioned here that similar studies have been conducted also before by SEMPA on antiferromagnetic Cr films on Fe(001) [24]. Spin-polarized scanning tunneling microscopy, which is presented in Sect. 3.6, is another method that can be used to image the surface spin structure of antiferromagnets [25, 26].

To summarize, SEMPA is a method that can provide real vectorial information about the sample magnetization distribution with high spatial resolution. The resolution is in principle determined only by the electron column, but since there is a certain trade-off between the intensity necessary for spin polarization detection and the resolution, in general the resolution of SEMPA does not exactly match that of scanning electron microscopy. It is a surface sensitive scanning technique. The sample has to be in ultrahigh vacuum, and the sample surface has to be clean and conducting. An advantage is also the variable field of view, which allows to zoom in and out in a quite wide range. SEMPA is not element-specific, and the size of the contrast may be weak for certain elements or surfaces. Since all the imaging is done by the primary electrons of relatively high energy, special set-ups have been developed and can be used to obtain SEMPA images even under moderate magnetic fields [27]. A deflection of the emitted electrons is not critical as long as there can be taken care that the electrons reach the spin detector.

3.4 Spin-Polarized Low-Energy Electron Microscopy (SPLEEM)

Instead of probing the sample with a finely focussed beam of unpolarized high-energy electrons and detecting the spin-polarization of low-energy secondary electrons, as in SEMPA, also the reverse approach is applicable for magnetic imaging. The reflection of spin-polarized low-energy electrons from a magnetic surface can strongly depend on the electron spin direction if, for example, the energy of these electrons matches a gap in the density of states above the vacuum level of either minority or majority electrons, but not of both [28]. The reflection of low energy electrons is enhanced in such gaps [29], which occur at zone boundary crossings in the extended zone scheme.

This can be implemented into a low energy electron microscope (LEEM) in the way shown in Fig. 9. LEEM is a parallel imaging technique, in which the sample is illuminated by a beam of low energy electrons, and the reflected electrons are used to create an image of the sample. As will be discussed below, imaging of emitted electrons is only feasible using immersion electron lenses as objective lens, in which a high voltage between sample and objective accelerates the electrons towards the imaging optics. The only way to get electrons as illumination onto the sample across the electric field in front

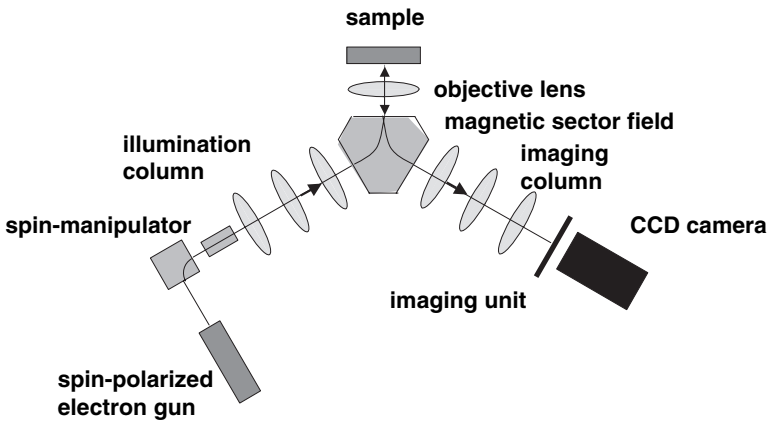

Fig. 9. Schematics of magnetic imaging by spin-polarized low-energy electron emission microscopy. Except for the spin-polarized electron gun and the spin manipulator at the left hand side, all other components are the same as for LEEM. An electron beam is formed in the illumination column, and deflected towards the sample by a magnetic sector field. It reaches the sample surface after passing through the objective lens. Reflected and emitted electrons from the sample are imaged by the objective lens, and deflected into the opposite direction by the magnetic sector field. The image is the projected by the imaging column on the imaging unit and recorded by a CCD camera

of the sample surface is to pass these electrons through the same objective lens. In a LEEM this is usually achieved by a magnetic sector field that acts as a beam separator. The Lorentz force (1) of a magnetic field acting on an electron contains the electron velocity vector, so that the deflection of the illuminating and the reflected electrons has opposite sign. The left part of the sketch of Fig. 9 is the illumination column. The only parts that are added for magnetic imaging are the spin-polarized electron gun and a spin manipulator, which will be described below. The right hand part is the imaging column, in which a parallel image of the sample by the emitted electrons is projected onto an imaging unit, usually a combination of an intensifying multi-channel plate and a fluorescent screen, from which the image can be read by a standard CCD camera.

The LEEM and later also the SPLEEM method were pioneered by E. Bauer and coworkers. Imaging of emitted electrons, though, is much older and dates back to the early work of Brüche in 1933 [30]. In order to obtain a reasonable intensity usually the so-called immersion or cathode lenses are used. Figure 10 shows a sketch of such a cathode lens. It shows an electric tetrode lens, which is called like that because it contains four optical elements. If you are now counting and think that the fourth element is missing in the drawing: It is not, the sample itself is the fourth element. By applying a high voltage between sample and objective lens, electrons are accelerated

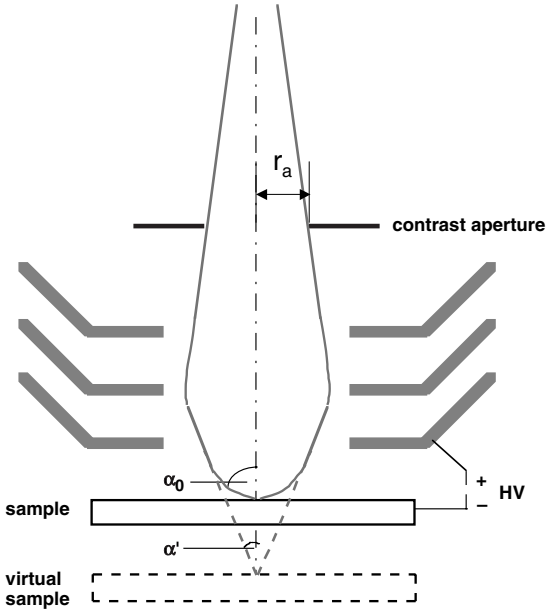

Fig. 10. Sketch of an electrostatic tetrode lens used for electron emission microscopy. Electrons are accelerated towards the entrance of the lens by a high voltage HV. Extrapolating straight rays makes them look like originating from a virtual sample under a virtual starting angle α', which is determined by the size r_a of the contrast aperture, and is much smaller than the real starting angle α_0

towards the entrance of the objective lens. This allows a higher solid angle of emitted electrons to be used for the imaging, and increases the intensity significantly. The electrons thus move on curved trajectories between the sample and the entrance of the objective lens. Optically it is equivalent to assuming that the electrons originate from a virtual sample at a larger distance from the objective lens, and under a virtual starting angle α' that is significantly smaller than the real starting angle α_0. These angles are determined by the contrast aperture that is placed in the back focal plane of the objective lens. By limiting its radius r_a and thus the angle α', spherical and chromatic aberrations can be reduced at the cost of reduced intensity. Magnetic cathode lenses reach theoretical resolutions below 10 nm for monoenergetic electrons and optimum aperture size. In practice, resolutions about a factor of 2–3 worse than the theoretical limit are achieved.

Figure 11 shows a sketch of the spin manipulator. It consists of a combination of electrostatic and magnetostatic electron deflectors, and is used to orient the spin polarization direction of the illuminating electron beam. Electrons that are emitted from the GaAs cathode of a spin-polarized electron gun are spin-polarized in the longitudinal direction, i.e., along the propagation axis. A 90° deflection of the electrons by an electric field preserves the

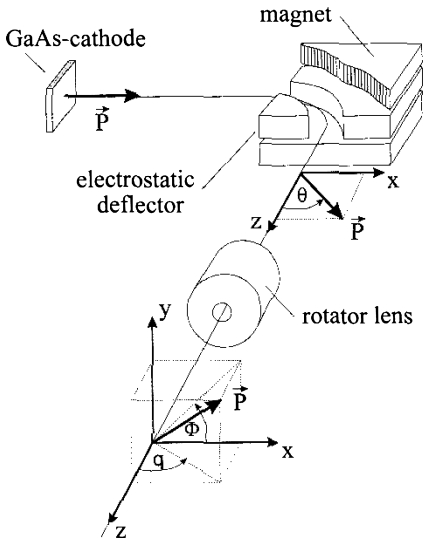

Fig. 11. Working principle of the spin manipulator for SPLEEM. Spin-polarized electrons with polarization vector pointing along x are emitted from a GaAs photocathode. The electron spin direction is preserved after an electrostatic 90° deflection, while it turns into the z direction after a magnetostatic 90° deflection. Any angle Θ between x and z can be selected by a combination of electric and magnetic fields. A subsequent magnetic rotator lens is used to rotate the spin out of the x–z plane by an angle Φ (Reproduced from [28] with permission, copyright (1998) by the World Scientific Publishing Company)

spin direction of the electrons, which are now transversely polarized along the x direction in the coordinate system of Fig. 11. On the other hand, if the 90° deflection is performed by a magnetic field, the electron spin is deflected along with the propagation direction, leading to a longitudinal spin polarization in the z direction. If the 90° deflection is achieved by a combination of electric and magnetic field, the resulting spin polarization can be adjusted at any angle Θ in the x–z plane. A rotation of the spin axis out of this plane is achieved by a second element, a magnetic rotator lens. A magnetic field along the electron propagation direction leaves the electron trajectory unchanged, but rotates the spin into the y direction. By a careful adjustment of all elements of such a spin manipulator the spin of the electrons illuminating the sample can thus be turned into any direction in space. This allows to obtain vectorial information by the SPLEEM technique. It should be mentioned that the spatial images obtained for different spin components are not a priori fully identical, like for SEMPA. While in SEMPA the selection of the spin component is done after the imaging process, in SPLEEM it is done before. Slight changes in the direction and angular spread of the electron beam by the spin manipulator may lead to slightly different spatial images. If the

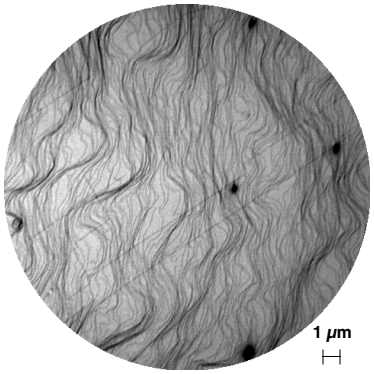

Fig. 12. Example of topographic contrast in LEEM. The image shows the (001) surface of a Cu single crystal. The *dark lines* represent monatomic steps [31]

spin manipulator is carefully adjusted, such deviations can be kept small, and magnetic images obtained for different components of the magnetization may still be compared numerically with each other.

An advantage of SPLEEM is that at the same time with the magnetic image, all the topographic and structural information of LEEM can be obtained. LEEM is a technique that is used by several groups for the study of single crystal surfaces and thin film growth. Figure 12 shows as an example a LEEM image of a Cu(001) surface [31]. The dark lines represent step edges between surface terraces of single atomic height. At some places these step edges are bunched together to form steps of a height of several atoms. The information obtained from LEEM images may be combined with the magnetic images from SPLEEM to identify structure–magnetism relationships on the nanoscopic scale.

The magnetic contrast in SPLEEM is realized by the spin-dependent reflection coefficient for low-energy electrons. The penetration of electrons into the sample is governed by the electronic states, and is smaller in gaps of the unoccupied part of the band structure [29]. Since bands of majority and minority electrons are shifted in energy with respect to each other, such gaps are located at different energies for the two spin directions. The spin-dependence of the reflection coefficient is the biggest at such spin-shifted gaps in the band structure [28]. The conditions for best magnetic contrast consequently change for different samples.

Figure 13 shows an example of a simultaneous structural and magnetic investigation by SPLEEM. Images (a)–(g) show the magnetic domain structure of an iron film at different times during the evaporation on a Cu(001) single crystal at room temperature. The curve in Fig. 13 is the simultaneously determined diffracted electron intensity, and reflects the atomic roughness of the surface [32]. Intensity oscillations are characteristic of a layer-by-layer growth of the Fe film, with maxima in the diffracted intensity corresponding

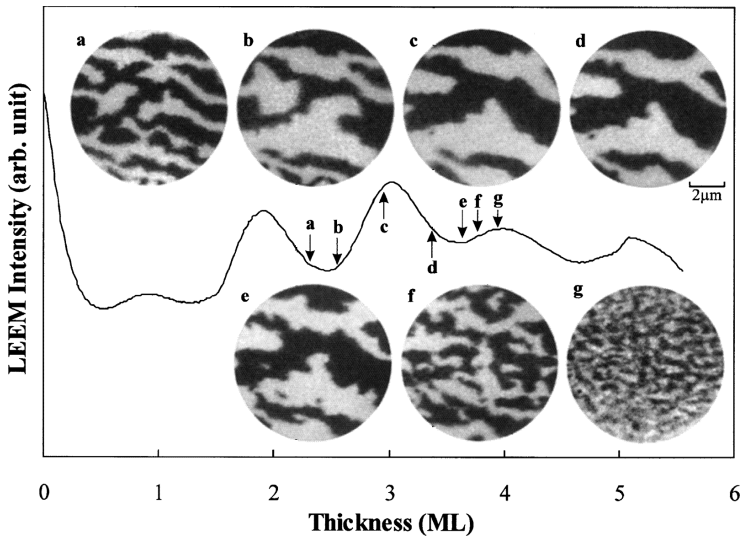

Fig. 13. Example of magnetic imaging by SPLEEM. The curve displays the diffracted electron intensity during the evaporation of Fe on Cu(001). Magnetic domain images (**a**)–(**g**) were taken during film deposition at the thicknesses indicated by arrows on the curve (Reproduced from [32] with permission, copyright (2001) by Elsevier Science)

to smooth surfaces. They appear in layer-by-layer growth at the completion of successive atomic layers, i.e., at film thicknesses of integer numbers of atomic monolayers (ML), and allow a precise thickness calibration of the deposited films. The total acquisition time of each image of Fig. 13 was only 10 s. Considering the low evaporation rate used in [32], this corresponds to the deposition of only 1% of a monolayer during acquisition of one image. Fe/Cu(001) exhibits a perpendicular magnetization in the thickness range of Fig. 13, leading to the occurrence of typical stripe domain patterns as discussed in Sect. 1, see Fig. 1 (d). From the series of images taken during growth of the Fe film the evolution of stripe patterns with different stripe width and shape can be clearly recognized, and correlated to the film thickness with extremely high accuracy.

In summary, SPLEEM is a technique that allows vectorial magnetic imaging at high lateral resolution. It is relatively surface sensitive, and has to be performed under high vacuum conditions. Because of parallel imaging and high electron intensities, it is a very fast technique, which allows real time magnetic imaging of, for example, growth-induced changes of the magnetic properties. A major advantage is that microscopic magnetic and topographic information can be obtained simultaneously. The conditions (electron energy) for best magnetic contrast depend on the sample, and have to be determined beforehand for best results. Since low energy electrons are imaged,

the technique is very sensitive to external magnetic fields. Only very small fields of a few Oersteds along the optical axis, i.e., perpendicular to the surface plane, may be tolerated if a special integrated coil design is used [33]. In general, however, it is necessary to image the remanent magnetic state of a sample. SPLEEM is not element-selective, and does not provide depth-selective magnetic information.

3.5 Synchrotron Radiation-Based Techniques

Synchrotron radiation-based techniques employ magnetic dichroisms in x-ray absorption as contrast mechanism for the magnetic imaging. The particular strength of these techniques is the elemental sensitivity of this magnetic contrast mechanism. X-ray magnetic circular dichroism (XMCD) relies on the spin-polarization of resonant transitions between occupied core states and spin-split unoccupied states just above the Fermi edge excited by circularly polarized photons. If the spin-polarization of the transitions, which is determined by the helicity of the exciting radiation, is aligned with the spin polarization of the unoccupied states, the absorption cross section is higher than in the opposite case, when the spin polarization of the transitions is antiparallel to the spin polarization of the unoccupied states. The photon energy at which this effect occurs depends on the binding energy of elemental core levels, and can therefore be used to probe different elements in a sample, or different magnetic layers containing different elements separately.

As in laterally integrating XMCD measurements, there are two basic ways of detecting the x-ray absorption. One can either detect the x-ray absorption by measuring the amount of emitted electrons at the sample surface, or by measuring the transmitted intensity of x-rays after transfer through the sample. In laterally integrating experiments the former is usually termed "total electron yield" detection of x-ray absorption. The latter is a more direct way of measuring the absorption, but requires appropriately thin samples.

In imaging experiments these two approaches are realized by combining resonant excitation by circularly polarized x-rays and existing microscopy techniques. A photoelectron emission microscope can be used to create a magnified image of the sample from the emitted electrons at the surface after photon absorption. In x-ray transmission microscopy an image of the sample is obtained from the locally different transmission of x-rays, which, if circularly polarized and tuned to elemental absorption edges, depends also on the local sample magnetization.

Photoelectron Emission Microscopy (PEEM)

We will first turn to the local electron yield detection of the x-ray absorption. Photoelectron emission microscopy (PEEM) is a relatively old technique, older than LEEM. Schematically it is similar to the imaging column of the

SPLEEM set-up presented in Fig. 9, but with a straight optics, since no deflecting magnetic sector field is necessary. As objective lens also the cathode lens type as the one shown in Fig. 10 or the magnetic counterpart are used. The first experimental realization by Brüche and Pohl dates back to the thirties [30, 34]. After adaption to ultrahigh vacuum environment [35, 36] PEEM was used in a number of studies of surfaces and surface reactions [37–40]. With the availability of synchrotron radiation sources and tunable x-rays the potential of PEEM for the spectromicroscopic detection of x-ray absorption was soon realized [41]; the first demonstration of magnetic contrast using XMCD as contrast mechanism followed a few years later [42]. XMCD-PEEM is routinely used as a technique for magnetic imaging since about 1997 [43–45].

Figure 14 shows an example of how magnetic contrast is obtained using XMCD [31]. Panel (a) shows the raw image of a Co/Ni bilayer on Cu(001), obtained with circularly polarized x-rays of positive helicity tuned to the

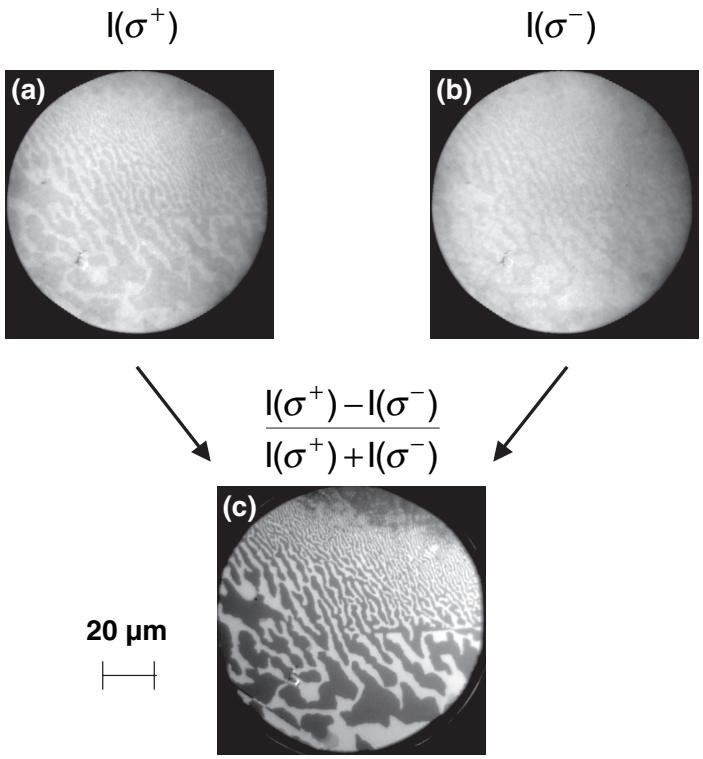

Fig. 14. Demonstration of magnetic contrast in XMCD-PEEM. (**a**): PEEM image of Co/Ni/Cu(001) obtained with circularly polarized x-rays of positive helicity at the Ni L_3 edge, (**b**): same with negative helicity. (**c**): Asymmetry image calculated from the images (a) and (b) showing the magnetic contrast

maximum of the Ni L_3 absorption edge. One can recognize a stripe-like contrast that is not observed in images taken for off-resonant photon energies. This is the magnetic contrast, representing the lateral distribution of XMCD. XMCD leads to a different x-ray absorption of domains with magnetization parallel and antiparallel to the helicity of the incoming x-rays. This is already visualized in the raw image (a), and seen in the live camera image. To prove the magnetic origin, the x-ray helicity can be reversed. Figure 14 (b) shows the same image, but for opposite x-ray helicity. Since all topographic contrast in the image does not depend on the x-ray helicity, all differences between images (a) and (b) are purely magnetic. It is seen that the stripe-like pattern indeed reverses its contrast, as is expected for magnetic contrast if the direction of the helicity vector is reversed. To eliminate all topographic contrast and obtain a magnetic domain image of the sample, the two images obtained for opposite helicity of the circularly polarized x-rays can be subtracted. Usually the result is then divided by the sum of the two images in order to eliminate effects of different illumination across the image. The result, the intensity difference $I(\sigma^+) - I(\sigma^-)$ divided by the sum $I(\sigma^+) + I(\sigma^-)$, is called asymmetry. It is presented in Fig. 14 (c). Dark and bright areas in that image correspond to domains of opposite magnetization, in the example of Fig. 14 to domains pointing into and out of the surface plane, because the thickness combination of Ni and Co in the Co/Ni bilayer was such that an out-of-plane easy axis resulted [31].

The stripe domains seen in Fig. 14 are typical for samples with an out-of-plane easy axis. As mentioned in Sect. 1 when discussing Fig. 1, these samples have a tendency towards domain formation. The demagnetizing energy connected to an out-of-plane magnetization direction can be lowered by formation of alternatingly magnetized domains, on the cost of exchange and anisotropy energy. The balance between these three energy terms, dipolar demagnetizing, exchange, and anisotropy energy, determines the width of the stripe domains. In Fig. 14 the stripe width shrinks across the range of the image from bottom to top. The reason is that the Co overlayer was deposited as a wedge with thickness increasing from bottom to top, which leads to a decrease in anisotropy energy and consequently to a decrease in domain size [31, 46].

In Fig. 14 the magnetization direction in the domains was known from the anisotropy of the sample, and confirmed by qualitative arguments about the shape of the domains. In general one does not know the magnetization direction from a single XMCD-PEEM image, but only the projection of the magnetization direction on the light helicity vector. Vectorial magnetic imaging as in SEMPA or SPLEEM would require to change the direction of the incoming synchrotron radiation with respect to the microscope. This would be evidently only possible by rotating or moving the vacuum chamber containing the PEEM; it has however not been realized to-date. Some instruments allow instead the azimuthal rotation of the sample, so that different

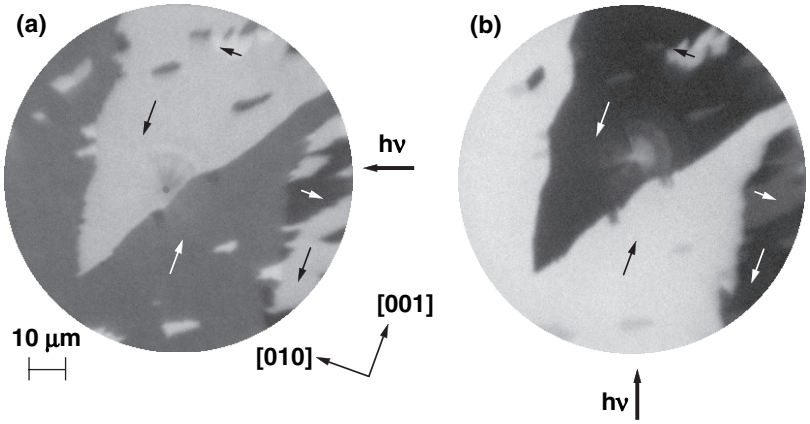

Fig. 15. Example of vectorial magnetic domain imaging using XMCD-PEEM. Magnetic domains in Fe/W(001) display different contrast depending on the azimuthal direction of the incoming x-rays, from the *right* in (**a**), from the *bottom* in (**b**). The local magnetization direction is indicated by arrows in some domains

light incidence directions with respect to the domain structure of the sample are possible. The imaging conditions in this case are not fully preserved after the rotation of the sample, since a tiny sample tilt or a minute asymmetric distortion of the electric field between sample and objective lens can cause slightly different image proportions or focusing conditions. Since the camera is not rotated together with the sample, it is also necessary to rotate the resulting image numerically. It is therefore normally not possible to compare images acquired for different sample azimuth numerically with each other, as it can be done in SEMPA or under certain conditions also in SPLEEM. What is possible, though, is a manual comparison of images for different light incidence in order to determine the magnetization vector in space. If the absolute value of the magnetization vector is known or can be assumed to be constant in different domains, two measurements, i.e., two images for different light incidence directions, are sufficient to determine the remaining two degrees of freedom of the magnetization vector in space. An example is given in Fig. 15. The two images (a) and (b) show magnetic domains of an Fe film on W(001) at about the same position of the sample [47]. The difference between the two images is the light incidence direction, which is indicated by arrows labelled "$h\nu$". Between the acquisition of the two images the sample was rotated by 90°, and afterwards the images were turned in the computer to display identical sample alignment. If one tries to overlay the images (a) and (b) of Fig. 15 it becomes evident that the domain boundaries do not match perfectly, and that the resolution is slightly better in panel (a) than in panel (b). From the manual quantitative comparison of the dichroic contrast in each of the domains, however, the magnetization direction can be determined. It is indicated by arrows in the larger domains. Four different

directions of magnetization are observed, corresponding to the four in-plane $\langle 100 \rangle$ crystallographic directions. It is nicely seen how the grayscale contrast varies with the different projections of these directions on the two different directions of light incidence. This works also for more complicated configurations in which the magnetization direction is not confined to the sample plane but exhibits in-plane and out-of-plane components [48, 49].

XMCD as an integral method is widely used in connection with a set of sum-rules [50, 51], which allow to extract quantitative magnetic information like the effective spin moment or the orbital moment per atom from a pair of x-ray absorption spectra for opposite helicity. If the photon energy is scanned in small steps and a stack of PEEM images is acquired for many different energies around the absorption edges for both helicities, a quantitative analysis of this microspectroscopic data set is possible. The result are microscopic images of the spin and orbital moments [52, 53].

As already mentioned in the introduction to Sect. 3.5, one of the main advantages of techniques using XMCD as contrast mechanism is the element-selectivity of the magnetic information. In samples that contain different magnetic layers of different elements this can be used for the layer-selective magnetic imaging. Nearly all of the most exciting new discoveries in thin film magnetism are observed in multilayered structures in which two or more magnetic layers have to be switched separately. To address the different layers separately and to obtain microscopic magnetic information about the different magnetic layers in a simple way is thus crucial for the microscopic investigation of such structures. With XMCD-based techniques this is possible by setting the x-ray monochromator of a soft x-ray beamline at a synchrotron radiation facility to the tabulated value of the photon energy corresponding to the elemental core–valence excitations. If the elemental composition of the multilayered structure is known, it is therefore straightforward to take images of the different layers. Figure 16 shows an example of layer-resolved magnetic images, taken at an FeNi/Cu/Co trilayer deposited on FeMn/Cu(001) [47]. It shows the layer-resolved magnetic domain structure after application of an external magnetic field of 340 Oe along the direction indicated by "H". Image (a) was obtained by tuning the photon energy to the energy of the Fe L_3 absorption edge, and thus represents the domain image of the FeNi top ferromagnetic layer, image (b) was acquired with the photon energy tuned to the Co L_3 absorption edge and shows the domain image of the Co bottom ferromagnetic layer. The domains in the Co layer are mainly oriented along two opposite $\langle 110 \rangle$ directions as indicated by arrows, namely along $[1\bar{1}0]$ and $[\bar{1}10]$, corresponding to dark gray and lighter gray contrast, respectively. Besides, there are also some small domains with brighter and darker contrast; they exhibit magnetization directions along [110] and $[\bar{1}\bar{1}0]$, respectively. The observed domain pattern in the Co layer was not changed by the application of the 340 Oe external field.

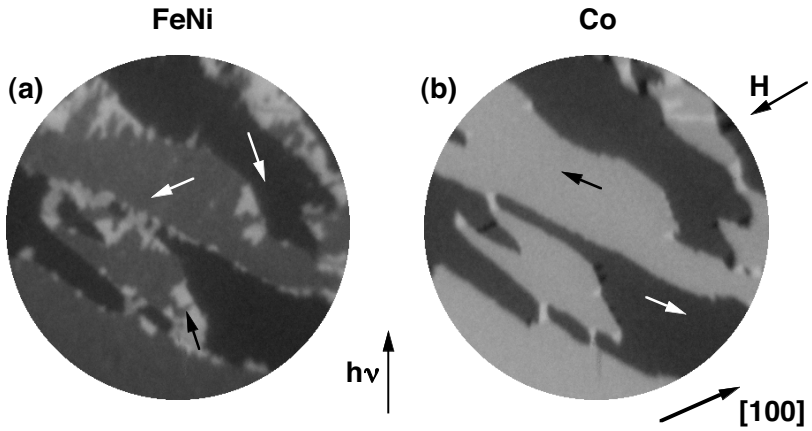

Fig. 16. Example of layer-resolved magnetic domain imaging by XMCD-PEEM. (**a**) and (**b**) show the magnetic domain images of the FeNi and the Co layer, respectively, of an FeNi/Cu/Co trilayer on FeMn/Cu(001) after application of an external magnetic field of 340 Oe in the direction indicated by "H". Domain walls in the Co layer are found to be decorated by small domains with bright contrast in the FeNi layer, pointing towards a local interlayer coupling mechanism mediated by the magnetostatic stray fields of domain walls

The domain image of the FeNi layer (a) shows a qualitatively similar pattern, but with different contrast. An analysis reveals that here the magnetization directions in the different domains are along the $\langle 100 \rangle$ in-plane directions, as indicated by arrows in some domains. The comparison with the domain image of the Co layer (b) shows that everywhere the magnetization directions of the two magnetic layers include an angle of 45°. This is explained by a different anisotropy energy in the two layers, and a parallel interlayer coupling [47]. Because of the direction of the applied field H, the magnetization in the FeNi layer points mainly along $[\bar{1}00]$ and $[0\bar{1}0]$. The interesting point in these images is that the positions of the domain boundaries of the Co layer are decorated in the FeNi layer by small domains with a brighter contrast, corresponding mainly to magnetization along [010]. This is an indication of a locally enhanced interlayer coupling at the domain walls of the Co layer. Such a local interlayer coupling has also been observed previously by XMCD-PEEM in Co/Cu/Ni trilayers, and is attributed to the interaction between the layers by the magnetostatic stray field emanating from the domain walls [54]. The identification and investigation of this coupling mechanism, which is highly relevant for the magnetization reversal and control of magnetic trilayers in devices, requires a technique that can provide microscopic lateral resolution and layer-resolved magnetic information at the same time. XMCD based methods do exactly fulfill such requirements.

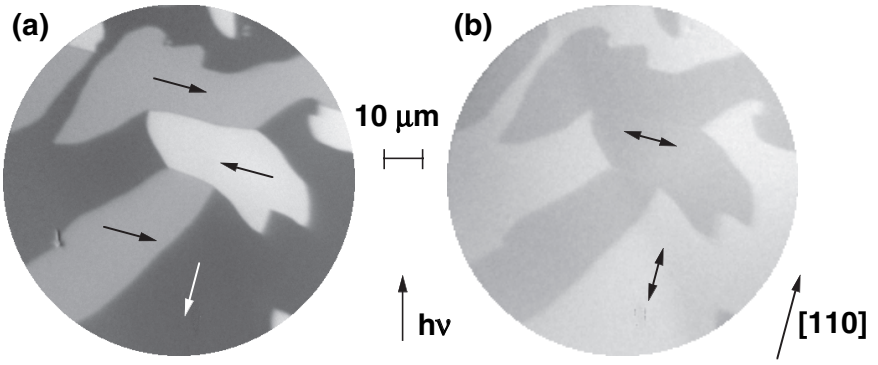

Fig. 17. Different magnetic contrast mechanisms for magnetic imaging by XMCD-PEEM. (**a**): "Conventional" magnetic imaging using x-ray magnetic circular dichroism (XMCD) as contrast mechanism. The graytone in the domain image is proportional to the projection of local magnetization direction on the incoming x-ray direction "$h\nu$". (**b**): Image at the same sample position obtained by x-ray magnetic linear dichroism (XMLD) as contrast mechanism. The graytone is proportional to the cosine square of the angle between the linear polarization axis of the incoming x-ray and the local magnetization direction

Although XMCD is the most widely used contrast mechanism for magnetic imaging with synchrotron radiation, also linearly polarized x-rays can be used to obtain magnetic contrast. The absorption of linearly polarized x-rays depends on the orientation of the electric field vector with respect to a uniaxial deviation from cubic symmetry of the electronic states involved in the transitions. Such a deviation can be caused by the presence of magnetic order. In that case absorption spectra for parallel and perpendicular alignment of polarization and magnetization axes show a typical plus/minus shaped difference at the absorption edges. This linear magnetic dichroism can be sizeable in oxides [55], but is much smaller in metals [56,57], typically more than a factor of 10 smaller than the circular dichroism. After a careful adjustment of the experiment and using an appropriate exposure time it still can be used for magnetic imaging. Figure 17 shows the comparison between magnetic domain images of a metal Co film on Cu(001) obtained by XMCD (a) and XMLD (b) [58]. Note that the span of the grayscale is not the same in (a) and (b), but has been adjusted to clearly show the magnetic domains. While the helicity vector of circularly polarized photons defines an orientation, the linear polarization vector defines only an axis. For symmetry reasons domains with opposite magnetization direction can therefore not be distinguished by linear magnetic dichroism, where the contrast follows a cosine-square behavior, and is maximum between domains with a 90° difference in magnetization direction. This is very nicely seen in Fig. 17, where in panel (b) the contrast between the bright and medium gray domains of panel (a) has vanished.

This property of XMLD, the insensitivity to the magnetization direction, allows to image domains in collinear antiferromagnets with different spin axes. A combination of XMCD- and XMLD-PEEM has indeed been successfully used to image antiferromagnetic domains in NiO [59] and $LaFeO_3$ samples [60,61], as well as their interaction with ferromagnetic domains of an adjacent ferromagnetic layer.

To be complete it should also be mentioned that dichroisms in photoelectron spectroscopy can be used for magnetic imaging, provided the instrument is equipped with an imaging energy filter to suppress the low energy secondary electrons and use only primary photoelectrons for the imaging process. In this case circular and linear magnetic dichroisms in photoemission lead to a magnetic contrast, the different angular behavior of which can deliver complementary information to XMCD-based magnetic images [62].

In summary, magnetic imaging by XMCD-PEEM provides element-selective magnetic domain images. The moderate surface sensitivity of the secondary electron yield detection of the x-ray absorption with an information depth of about 2 nm [63] allows to image also buried layers and interfaces close to the surface. PEEM has a good resolution, however using it in connection with synchrotron radiation increases the chromatic aberrations so that the attainable resolution is somewhat worse compared to LEEM. It is a parallel imaging method that has to be performed in vacuum, although not necessarily in ultrahigh vacuum. Vectorial information can be obtained manually by analyzing images obtained for different sample azimuth angle. Since low energy electrons are imaged, it is very sensitive to external magnetic fields, and allows only images of the remanent magnetic state of a sample. In connection with microspectroscopic data the quantitative magnetic information inherent to XMCD spectra can be combined with lateral resolution. Synchrotron radiation is needed.

Magnetic X-ray Transmission Microscopy (M-XTM)

Magnetic x-ray transmission microscopy is the transmission counterpart to XMCD-PEEM for the laterally resolved detection of XMCD. It is performed either by parallel imaging, or by scanning. X-ray transmission microscopes are mostly used to image biological systems with high resolution using synchrotron radiation x-rays. X-ray microscopes work with zone plates as x-ray lenses. Zone plates are tiny lithographically fabricated concentric ring structures in which the width of the alternating open and closed circles varies as a function of the radius. These rings give rise to a diffraction of the x-rays. In order to focus the first order diffraction of a parallel x-ray beam into a common focal point, the diffraction angle has to be larger for rays that are further away from the optical axis. This is achieved if the ring width is inversely proportional to the radial position from the center. Because the diffraction angle depends on the wavelength, the focal length is proportional to the x-ray photon energy. The attainable resolution of a zone plate is determined by the

width of the outermost ring. With state-of-the-art lithography a resolution of 20 nm and below can be achieved.

A sketch of a set-up of a transmission x-ray microscope for parallel imaging is shown in Fig. 18 [64]. A condenser zone plate focusses the illuminating x-rays onto the sample. A microscopic image of the transmitted intensity is created by an objective zone plate ("micro zone plate" in Fig. 18) behind the sample, where it is read by an imaging unit, for example a CCD chip. In a scanning transmission x-ray microscope a focussed x-ray beam is created by a zone plate optics in front of the sample, the sample is moved by a piezo scanner, and the transmitted x-ray intensity behind the sample is recorded by an integral x-ray detector as a function of sample position. The distance between the sample and zone plate is quite small, and usually transmission x-ray microscopy is not performed under ultrahigh vacuum conditions.

In the set-up shown in Fig. 18, where the x-rays reach the sample under normal incidence, the magnetic contrast in the resulting image represents only the out-of-plane component of magnetization. Sensitivity to in-plane components can be achieved by a modification of the XTM set-up so that the sample can be tilted with respect to the optical axis [65]. Since the focal length of a zone plate depends on the wavelength of the x-rays, the distances between zone plates, sample, and detector have to be re-adjusted if a different photon energy is to be used.

Compared to PEEM, the detection of XMCD by TXM differs in several ways: The resolution is usually higher in TXM, but the field of view can not be easily changed. Since TXM is a photon-in/photon-out method, it is not sensitive to external magnetic fields. It is thus ideally suited for the imaging of magnetization reversal processes, for example in small magnetic structures. The main difference between M-TXM and XMCD-PEEM, however, is the way the magnetic information is obtained. XMCD-PEEM is an on-surface

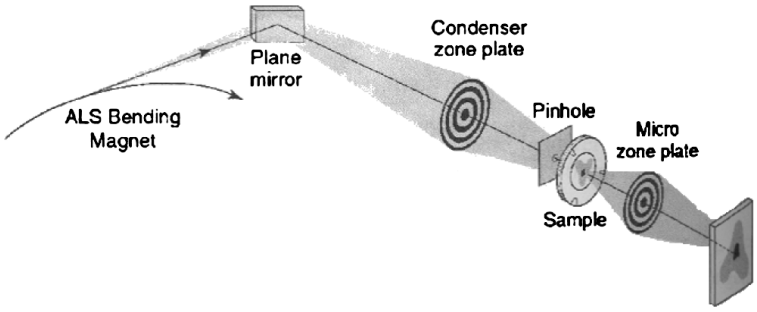

Fig. 18. Schematics of a transmission x-ray microscope. The x-ray beam from a synchrotron radiation source is focussed onto the sample by the condenser zone plate. A magnified image of the transmitted intensity is projected onto a detector by the micro zone plate (Reproduced from [64] with permission, copyright (2001) by IEEE)

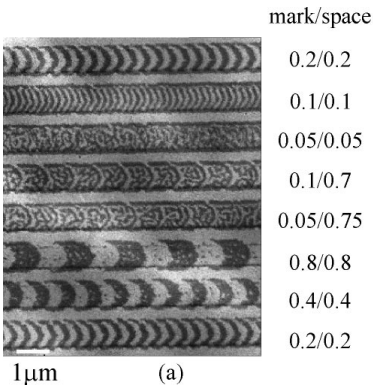

Fig. 19. Example of magnetic domain imaging using a transmission x-ray microscope showing a test pattern in a $Tb_{25}(Fe_{75}Co_{25})_{75}$ film for magneto-optical data storage. The mark/space assignments of the different stripe patterns are given in μm (Reproduced from [66] with permission, copyright (2001) by the American Institute of Physics)

technique with a probing depth of about 2 nm, while TXM is a transmission method. PEEM is thus more sensitive for signals of ultrathin films or interfaces, while information from more deeply buried layers (below $\approx$ 10 nm) is only obtained by M-TXM. Substrates for M-TXM have to be suitably chosen membranes.

Figure 19 shows an example of magnetic imaging by magnetic x-ray transmission microscopy. Displayed is a magnetic domain image of a 50 nm thick $Tb_{25}(Fe_{75}Co_{25})_{75}$ magneto-optical storage media with out-of-plane easy axis, in which test patterns with different bit sizes and periods have been written. It shows that the thermally assisted write process works well for periods of 200 nm and higher, while it fails for smaller bits or smaller bit spacings [66].

3.6 Scanning Probe Techniques

In scanning probe techniques a sharp tip is laterally moved above the sample surface. The size of an interaction between tip and sample is measured, and usually a feedback loop is used to adjust the tip height in such a way to keep the strength of this tip-sample interaction constant. Depending on the type of tip-sample interaction several different scanning probe techniques can be distinguished. Prominent examples are scanning tunneling microscopy (STM), in which the size of the tunnel current between the tip and a conducting sample represents the tip-sample interaction, and atomic force microscopy, in which either the repulsive binding force upon close approach between tip and sample, or van der Waals forces at larger distances are used to regulate the tip-sample distance. In the following two scanning probe techniques for magnetic imaging that are based on these two non-magnetic imaging

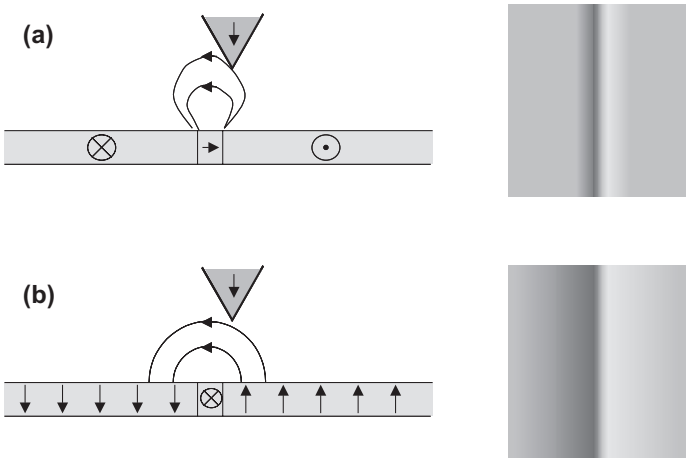

Fig. 20. Schematic explanation of the contrast in magnetic force microscopy. (**a**): Thin film sample with in-plane magnetization. The stray field originating from a Néel wall between two domains with opposite magnetization direction leads to a black/white contrast in the MFM image (*right*). (**b**): Thin film sample with out-of-plane magnetization. The stray field originating from the edges of the domains leads to a contrast as schematically displayed at the right

techniques are presented. As magnetic tip-sample interaction serve the force between the stray field of the sample and a magnetic tip in one case, and the spin-dependence of the tunnel current in the other.

Magnetic Force Microscopy (MFM)

Magnetic force microscopy (MFM) is one of the most widely used techniques for magnetic imaging. This is due to the easy implementation of MFM into the existing scanning probe technology, the high resolution, and the insensitivity to the surrounding which makes MFM applicable also under ambient pressure. In MFM the force exerted on a magnetic tip by the stray field of the sample above the surface is measured. State-of-the-art atomic force microscopes are able to detect very small forces between sample and tip by a change in resonance frequency of a cantilever on which the tip is mounted. This can be used also for the detection of the small magnetic forces that occur when the tip is positioned above the sample surface. MFM is an indirect imaging technique, since not the magnetic domains, but the stray fields above the surface of the magnetic domain pattern are imaged.

Figure 20 shows schematically the working principle of MFM. In the upper panel (a) a situation is considered in which two oppositely magnetized domains in a thin film are separated by a Néel wall. Magnetic poles at both ends of the domain wall lead to a stray field outside the sample as indicated by arrows. If a magnetic tip with magnetization direction as sketched in Fig. 20

(a) is moved across the domain wall, it will experience a repulsive force on the right side of the domain wall, and an attractive force on the left side. An image of the cantilever oscillation frequency would qualitatively look like the one shown on the right hand side, where a brighter contrast means a higher oscillation frequency, corresponding to a repulsive force.

The case of a sample with out-of-plane magnetization is sketched in Fig. 20 (b). An infinitely extended sample with a single domain with perpendicular magnetization does not exhibit a stray field outside the sample, since the magnetic flux density is completely closed inside the film by the demagnetizing field, as discussed in Sect. 1. However, at the domain boundaries part of the flux is also closed outside the sample, as sketched in Fig. 20 (b). This part of the flux is actually exactly the one responsible for the reduction of the demagnetizing energy, which leads to the occurrence of stripe domains in films with perpendicular anisotropy. For MFM this means that close to the domain walls there is a magnetic force acting on the tip. As in the case of the Néel wall in panel (a), the perpendicular component of this force changes sign at the center of the domain wall, resulting in an image as depicted at the right. If the width of the stripe domains is similar to the tip-sample distance, typically about 50 nm or more, the domains appear with a constant alternating contrast in the final image. In this case it looks like an image of the sample magnetization, but one should keep in mind that magnetic images obtained by MFM do not directly represent the magnetization distribution of the sample, but contain only indirect information about it. The actual domain pattern has to be reconstructed from the force images. In the case of narrow out-of-plane domains this is quite easy, but can be more complicated for in-plane domains with different magnetization angles. The long range nature of dipolar interactions is an additional obstacle. In addition, the interaction of the stray field of the tip may influence the sample magnetization in soft magnetic samples. An example is shown in Fig. 21. It shows in panels (b) and (c) MFM images of a $2 \times 2\ \mu m^2$ permalloy microstructure of 16 nm thickness, taken for opposite tip magnetization direction. The arrows in panel (a) show the result of a micromagnetic simulation for this structure, while the grayscale represents the simulated MFM contrast resulting from this calculated magnetization distribution. As schematically shown in Fig. 1 (b), the energetically most favorable state in square microstructures of a certain size is the so-called Landau pattern, in which no flux exits at the sample's outer edges. At the 90° domain boundaries, however, some flux is present above and below the structure. This is imaged by the MFM, where it leads to the typical black/white contrast at these lines. The sequence of black and white is reversed if the tip magnetization is reversed, which is clearly recognized in Fig. 21. Compared to the simulated pattern (a), however, the experimentally observed domain patterns (b) and (c) exhibit a more curved appearance of the domain walls. Furthermore, the curvature is different in (b) and (c). It is

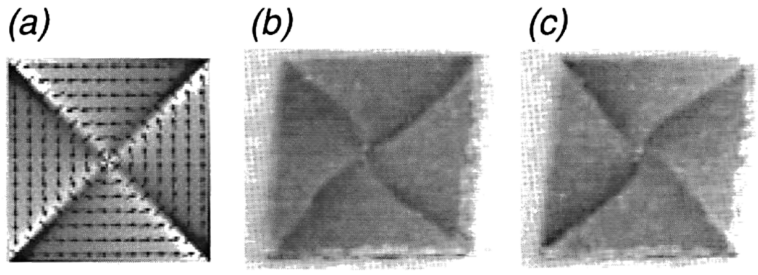

Fig. 21. Example of magnetic imaging using MFM. (**a**) Micromagnetic simulation of a $2 \times 2\ \mu m^2$ permalloy element of 16 nm thickness. (**b**), (**c**): MFM images of this element obtained with opposite tip magnetization directions. From [67]

attributed to the perturbation of the sample magnetization distribution by the stray field of the tip [67].

Although the information about the magnetization distribution in a sample is only indirect, MFM is nevertheless probably the most widely used technique for magnetic imaging. Reasons are the high resolution, which until shortly made MFM a standard technique in development and production of magnetic storage devices, the easy use under environmental conditions (no vacuum necessary), and the commercial availability of instruments. Another advantage of MFM is that within the same instrument also topographic information can be obtained from the atomic force mode of operation. If the magnetization reversal of the tip is taken into account, MFM tolerates quite high external fields, and allows the study of magnetization reversal processes.

The lateral resolution depends on the distance between tip and sample, and on the shape of the tip. Routinely about 50 nm are achieved. To improve the resolution, both the design of the tip and the method of tip-sample distance control have to be worked on [68]. Although MFM does not directly provide quantitative information, several attempts for quantitative calibration of MFM have been performed [69–72]. This is not straightforward since also the shape and the magnetization distribution of the tip enter in the equations for the force. A calibration of the tip properties with a known sample is therefore indispensable for obtaining quantitative information from MFM. MFM is not element-selective. Due to the long-range nature of the dipolar interaction also information from deeper layers of a sample is obtained, but it may be sometimes difficult to single out the contributions to the force coming from certain depths of a sample.

Spin-Polarized Scanning Tunnelling Microscopy (Sp-STM)

The other tip-sample interaction that is being used for magnetic imaging is the size of the electron current tunnelling through the vacuum gap between a metallic tip and the sample. The tunnel current between two magnetic electrodes depends in general on the relative orientation of the two magnetization

directions. This is explained by Fig. 22. It gives a schematic representation of the involved spin-split densities of states. The left graph shows the spin-resolved density of states of the sample. The horizontal line is the Fermi edge. Majority and minority states are shown left and right of the vertical energy axis, respectively. The middle graph shows the density of states of a tip that is magnetized parallel to the sample. The applied bias voltage U_{bias} between sample and tip appears as an energy difference between the Fermi levels of sample and tip. Since the electron spin is preserved in the tunnel process, tunnelling occurs between majority states of the tip and majority states of the sample, as well as between minority states of the tip and minority states of the sample. For a positive bias voltage as drawn in Fig. 22, electrons tunnel from occupied states of the tip into unoccupied states of the sample. The graph on the right hand side of Fig. 22 shows the density of states of the tip if its magnetization direction is reversed, i.e., if majority and minority states are exchanged. In this case, when tip and sample magnetizations are antiparallel, minority electrons from the tip can tunnel into majority states of the sample, and vice versa. The tunnel current in these two cases, tip magnetization parallel or antiparallel to the sample magnetization, will generally be different. This is called tunnel magnetoresistance [73], and can be used to obtain information about the sample magnetization in a scanning tunnelling microscopy experiment.

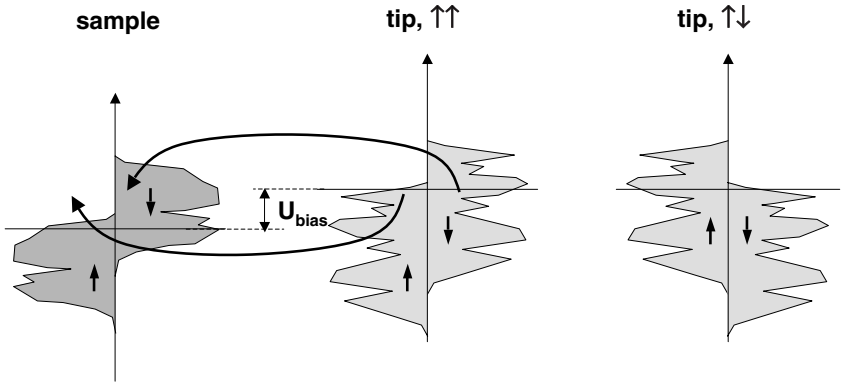

Fig. 22. Schematic explanation of tunnelling magnetoresistance between a magnetic tip and the sample in scanning tunnelling microscopy. *Left*: spin-split density of states of the sample, *middle*: spin-split density of states of a tip with magnetization parallel to that of the sample, *right*: spin-split density of states of a tip with magnetization antiparallel to that of the sample. Electron tunnelling occurs between states of tip and sample of the same spin direction. Separation between magnetic and topographic contrast can be obtained by using a lock-in technique and modulating either the tip magnetization direction or the bias voltage between tip and sample

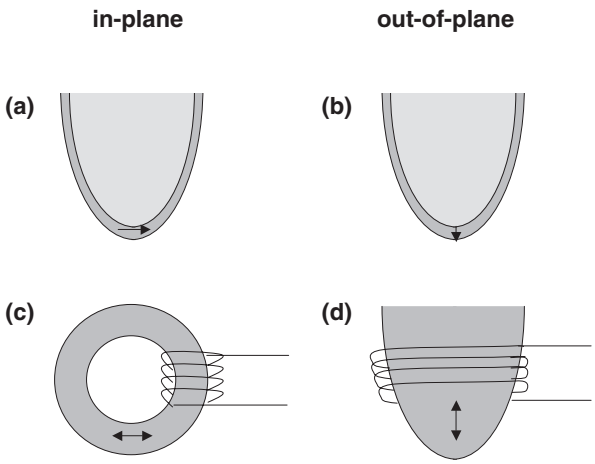

Fig. 23. Schematics of different ways of experimental realization of spin-polarized scanning tunneling microscopy. (**a**), (**b**): Tip covered by a magnetic thin film, used for sp-STM by modulating the bias voltage between tip and sample. (**c**), (**d**): Bulk tips used for sp-STM by reversing the tip magnetization. (a) and (c) show geometries with sensitivity for in-plane magnetization, (b) and (d) geometries with sensitivity for out-of-plane magnetization

The great difficulty is that besides this dependence on the relative orientation of sample and tip magnetization the tunnel current also depends exponentially on the distance between tip and sample. This is the normal contrast mechanism used in STM to obtain topographic contrast. If one wants to use the tunnel magnetoresistance as contrast mechanism for magnetic imaging, the task is to separate magnetic from topographic signal in the tunnel current. This has to be done at each position in an image independently, since the large change in tunnelling current when moving the tip across the sample surface does not allow any conclusions about the magnetic contribution. It has been accomplished by two different approaches. The magnetic signal can be identified by modulating a parameter and using a lock-in technique to separate the much smaller magnetic signal from the topographic signal. In the two different approaches the parameter to be modulated was in one case the bias voltage, in the other the direction of tip magnetization. These two ways of realizing sp-STM are shown in Fig. 23. The top row shows a tip covered with a thin magnetic film. Depending on the magnetic anisotropy of the film, the magnetization at the tip apex will be either perpendicular to the tip axis (a) or along the tip axis (b), probing thus samples with in-plane or out-of-plane magnetization, respectively. Using such a tip, the bias voltage U_{bias} has to be modulated. The lock-in signal will then yield the energy derivative of the tunnel current, which, like the tunnel current itself, will in general depend on the relative orientation of tip and sample magnetization. It is then possible to use the magnitude of the tunnel current to control the

tip-sample distance, and the lock-in signal to obtain information about the sample magnetization. This spectroscopic approach has been pioneered by Bode, Wiesendanger, and coworkers [25, 74]. The problem is that the magnetic signal varies in size as a function of bias voltage, and that different elements will also lead to a different dI/dU_{bias}. The advantage is that once a tip is covered with a magnetic film it is easily implemented into any existing STM. It is also possible to use antiferromagnetic tips in order to make the technique more insensitive to the application of external fields [75].

The other approach, modulating the tip magnetization, is shown in Fig. 23 (c) and (d). It was pioneered by Wulfhekel, Kirschner, and coworkers [76,77]. Here the tip has to be fully made from a magnetic material. The tip magnetization is then periodically reversed by the current through a coil. For a normal tip (d) this leads to a sensitivity to the out-of-plane component of magnetization. Note that according to the scale the tips are sketched in Fig. 23, the coil would be way up and much larger. To detect in-plane components, a special ring-like design of the tip (c) has to be used in order to reverse the magnetization direction [78]. Here the electrons tunnel between the sample and the bottommost atoms of a tiny washer-like ring. Modulating the sample magnetization yields directly the tunnel magnetoresistance from the lock-in output. The signal in this method is present and can be used for magnetic imaging at any bias voltage, which is an advantage in particular if the spectroscopic properties of a sample are not known beforehand. Technical problems are the choice of an appropriate tip material, which has to be magnetically soft and at the same time exhibit very low magnetostriction.

An example of magnetic contrast by sp-STM is shown in Fig. 24. Like for SEMPA, the high surface sensitivity of Sp-STM allows the investigation of layered antiferromagnetic samples. This has been successfully used for the imaging of Cr(001) [25] and Mn/Fe(001) [26, 78]. Figure 24 gives an example from [78]. Panel (a) shows the topographic STM image of 7 ML Mn on an Fe(001) single crystal. Black, gray, and white contrast corresponds to increasing terrace height in steps of one atom. Figure 24 (b) shows the simultaneously acquired magnetic signal, using the technique as sketched in Fig. 23 (c). Now the different grayscales correspond to different local magnetoresistance between tip and sample. Comparing Figs. 24 (a) and (b), the layered antiferromagnetic spin structure of the Mn film is nicely recognized, similar to the example shown in Fig. 8.

Sp-STM is at present the magnetic imaging technique with the highest resolution, less than 1 nm. It is very surface sensitive, and has to be performed under ultrahigh vacuum conditions. Topographic information as in STM is available from the same measurement. The high surface sensitivity implies that the signal from buried layers is not accessible by Sp-STM.

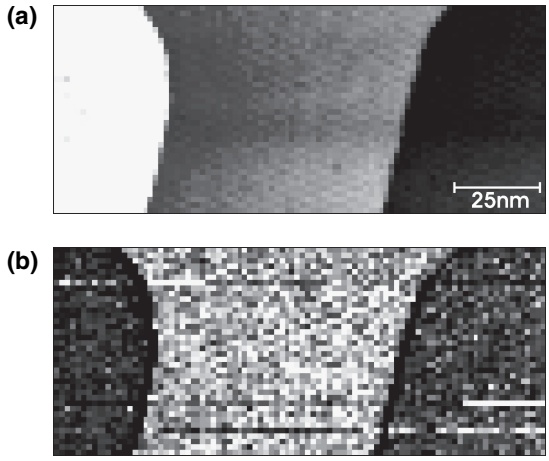

Fig. 24. Example for magnetic imaging by sp-STM. (**a**): Topographic STM image of a Mn film of 7 ML thickness on Fe(001). (**b**): Magnetic sp-STM image at the same position of the sample, acquired simultaneously with the topographic information (Reproduced from [78] with permission, copyright (2003) by the American Institute of Physics)

4 Summary and Outlook

The features of the various techniques for magnetic imaging that have been presented in the previous chapters are summarized by pictograms in Table 2. The first column, headed by a magnifying glass, refers to the resolution. The resolution of the listed techniques ranges between that of Kerr microscopy (500 nm) and sp-STM (< 1 nm), the latter being characterized by a double smiley. Due to the chromatic aberration, the resolution of XMCD-PEEM is somewhat worse compared to SPLEEM despite the identical electron imaging technique.

The second column, headed by an hourglass, gives an overview of the speed of image acquisition. Although the speed depends on image size, resolution, and the actual system under study, in general the scanning probe techniques and SEMPA as scanning technique with the intensity loss in the spin detection process have to be considered as relatively slow. The type of image acquisition, scanning or parallel imaging, is listed in the third column, titled with an eye symbol. The magnifying glass pictograms indicate parallel imaging, while the page with lines pictogram refers to scanning imaging.

An important point is the sensitivity to external magnetic fields. This is summarized in the fourth column, headed by a horseshoe magnet symbol. Here the techniques that use low energy secondary electrons for the imaging as SPLEEM and XMCD-PEEM are marked by bomb symbols, indicating a high sensitivity to external magnetic fields. In SEMPA also slow electrons are detected, but they do not form the image, which is determined by the

Table 2. Summary of the features of the discussed magnetic imaging techniques. Columns with pictograms refer (from left to right) to resolution, image acquisition speed, type of imaging (parallel imaging or scanning), sensitivity to applied magnetic fields, type of depth information (surface based or transmission), information depth (path length for exponential weighting for surface based techniques, maximum sample thickness for transmission techniques), possibility to obtain depth selective information

Kerr microscopy	☹	☺		☺		< 20 nm	😐
Lorentz microscopy	☺	😐		😐		< 100 nm	☹
SEMPA	☺	☹		☹		< 0.5 nm	
SPLEEM	☺	☺				< 1 nm	
XMCD-PEEM	😐	☺				< 5 nm	☺
M-TXM	☺	☺		☺		< 200 nm	☺
MFM	☺	☹		☺		< 2 μm	☹
sp-STM	☺ ☺	☹		☺ ☹		< 0.2 nm	

high energy primary electrons, so that moderate magnetic fields can be tolerated in certain dedicated set-ups. Two different symbols are shown in the field for sp-STM. They refer to the two different experimental approaches: If the magnetization of a soft magnetic tip is being modulated, sensitivity to external magnetic fields is higher than in the approach where the sample bias voltage is modulated.

The fifth column, with a rectangular box as title, displays the way the magnetic information is obtained. The different pictograms found in that column indicate on-surface acquisition and transmission measurements, respectively. Modified on-surface symbols are being used for the scanning probe techniques MFM and sp-STM, to indicate that the surface is not, as in the other techniques, probed by an incident electron or photon beam. The approximate corresponding length scales, information depth in the case of on-surface measurements, and maximum sample thickness in the case of transmission measurements, are listed in the sixth column, titled with a distance pictogram.

The last column summarizes another important aspect of magnetic imaging techniques, namely the possibility to obtain depth-resolved information, for example in multilayered magnetic samples. This is most easily achieved by the XMCD-based techniques, XMCD-PEEM and M-TXM, which due to their element-selectivity can address different magnetic layers at different depths separately. A depth sensitivity can also be achieved in Kerr microscopy by a careful adjustment of the phase. Lorentz microscopy as a transmission

technique provides information from all depths of a sample; with some additional information at hand, features in the final image may be attributed to different layers at different depths. The same holds for MFM, which due to the long-range dipolar interaction provides also information about magnetic domain walls in more deeply buried layers. No depth-resolved information is available from images of the more surface-sensitive techniques like SEMPA, SPLEEM, and sp-STM.

A trend that has already started is to furnish magnetic imaging with time resolution to obtain laterally resolved images of the dynamic magnetic response of the sample. Especially with respect to the increased data rate in magnetic data storage the dynamic behavior of small magnetic structures is becoming more and more important. Time-resolution has been successfully integrated into scanning Kerr microscopy in a stroboscopic pump–probe approach [79–81]. Since a laser beam is used for the illumination of the sample, it is quite straightforward to include the time structure of a pulsed laser source for the probe in a pump–probe scheme. The pump has to be an ultrashort synchronized magnetic field pulse, which can be obtained by hitting a photoconductive switch with a laser pulse, and passing the generated current pulse through a stripline underneath the sample.

Similar time-resolved pump–probe experiments have also been already implemented in synchrotron radiation-based magnetic imaging techniques. Here the pulsed time structure of the synchrotron radiation provides the probe. Compared to a laser pulse the typical width of a synchrotron radiation pulse is much larger, typically about 50 ps, but still smaller than typical rise times in stripline-generated magnetic field pulses. Stroboscopic time-resolved magnetic imaging has been demonstrated in XMCD-PEEM by several groups [82–85], and also in M-XTM [86]. The element-selectivity of XMCD is an advantage also for the time-resolved measurements, since magnetization reversal dynamics of the different magnetic layers in a magnetic trilayer can be studied separately [87].

The electron imaging techniques like SPLEEM and XMCD-PEEM, but also Lorentz microscopy, may benefit in the near future from novel developments for aberration correction. In light optical lens systems aberration correction is accomplished by suitable combinations of convex and concave lenses. Since there are no concave lenses for electron imaging, aberration correction can not readily be performed in electron optics. The first suggestion for an aberration-corrected electron optics by non-rotational-symmetric lenses has been made by Scherzer more than half a century ago [88]. 43 years later Rose took up the idea [89], which lead to the construction of an aberration corrected transmission electron microscope [90]. An aberration correction scheme for LEEM and PEEM based on the reflection of electrons in a tetrode electron mirror was also suggested [91], and currently two experimental realizations of aberration-corrected instruments are under development at BESSY in Berlin [92] and at the ALS in Berkeley. The theoretical resolution

is expected to be better than 1 nm; in addition, a huge increase in intensity is expected compared to non-corrected instruments for identical resolution settings because a bigger contrast aperture can be selected in the corrected instrument, which leads to a larger electron acceptance angle (cf. Fig. 10).

New developments in the so-called "lensless imaging" should be also mentioned here, although strictly speaking this is not an imaging technique but belongs to the class of diffraction experiments. A collaboration of researchers from BESSY and the ALS/Stanford University achieved the holographic reconstruction of a magnetic domain image from a resonant x-ray scattering experiment using coherent x-ray radiation in combination with the XMCD effect [93, 94]. In their set-up a coherent x-ray beam, tuned to an elemental absorption edge of the sample, was transmitted through a thin magnetic film with out-of-plane magnetization. The diffraction pattern of a small reference hole next to the sample was superimposed for phase retrieval. The resulting coherent scattering speckle pattern was then recorded. This allows the reconstruction of the magnetic real-space image [93, 94]. It is expected that this way of magnetic imaging will greatly benefit from the availability of free electron based sources of extremely brilliant and ultrashort x-ray pulses.

The new developments mentioned in this section have just begun. Together with other improvements on the existing magnetic imaging methods they will push the whole field forward, and open new ways for the investigation of magnetic properties for both fundamental and applied research. This is necessary since the shrinking dimensions of structures involved in magnetic recording and data storage technology pose a serious challenge to the resolution and the speed of magnetic imaging techniques. Magnetic imaging can only be competitive if the resolution satisfies the needs. On the other hand this is a big chance, since it increases the quest for microscopic information to understand the fundamentals of dynamic micromagnetism in confined structures.

Acknowledgement

My thanks go to L.I. Chelaru, K. Fukumoto, F. Offi, J. Wang, M. Kotsugi, C. Quitmann, F. Nolting, T. Ramsvik, and J. Kirschner for the collaboration on results presented in Sect. 3.5 of this chapter. This research has been partly financed by the BMBF (grant no. 05 KS1EFA6). I am grateful to W. Wulfhekel, U. Schlickum, and H.P. Oepen for critical reading of parts of the manuscript. Finally I also want to thank the organizers of the IVth International School on Magnetism and Synchrotron Radiation in Mittelwihr (France) for the invitation to present the above lecture.

References

1. H. Hopster, H.P. Oepen (Eds.): *Magnetic Microscopy of Nanostructures*, (Springer, Berlin Heidelberg New York 2004)
2. D.P. Pappas, K.-P. Kämper, H. Hopster: Phys. Rev. Lett. **64**, 3179 (1990)
3. D.P. Pappas, C.R. Brundle, H. Hopster: Phys. Rev. B **45**, 8169 (1992)
4. Z.Q. Qiu, J. Pearson, S.D. Bader: Phys. Rev. Lett. **70**, 1006 (1993)
5. R. Allenspach, A. Bischof: Phys. Rev. Lett. **69**, 3385 (1992)
6. M. Speckmann, H.P. Oepen, H. Ibach: Phys. Rev. Lett. **75**, 2035 (1995)
7. K. Fukumoto, H. Daimon, L.I. Chelaru et al.: Surf. Sci. **514**, 151 (2002)
8. A. Hubert, R. Schäfer: *Magnetic Domains*, (Springer, Berlin Heidelberg New York 1998)
9. L.D. Landau, E.M. Lifshitz: *Electrodynamics of Continuous Media*, (Pergamon, London 1960)
10. S.D. Bader: J. Magn. Magn. Mater. **100**, 440 (1991)
11. R. Schäfer: J. Magn. Magn. Mater. **215-216**, 652 (2000)
12. R. Schäfer, R. Urban, D. Ullmann et al.: Phys. Rev. B **65**, 144405 (2002)
13. M. de Graef: Lorentz Microscopy: Theoretical basis and image simulations. In: *Magnetic imaging and its applications to materials*, ed by M. de Graef, Y. Zhu (Academic Press, San Diego 2001) pp 27–67
14. A.K. Petford-Long, J.N. Chapman: Lorentz Microscopy. In: *Magnetic Microscopy of Nanostructures*, ed by H. Hopster, H.P. Oepen, (Springer, Berlin Heidelberg New York 2004) pp 67–86
15. M. Herrmann, S. McVitie, J.N. Chapman: J. Appl. Phys. **87**, 2994 (2000)
16. G.R. Morrison, J.N. Chapman: Optik **64**, 1 (1983)
17. G.R. Morrison, H. Gong, J.N. Chapman et al.: J. Appl. Phys. **64**, 1338 (1988)
18. J. Unguris: Scanning electron microscopy with polarization analysis (SEMPA) and its applications. In: *Magnetic imaging and its applications to materials*, ed by M. de Graef, Y. Zhu (Academic Press, San Diego 2001) pp 167–193
19. H.P. Oepen, H. Hopster: SEMPA Studies of Thin Films, Structures, and Exchange Coupled Layers. In: *Magnetic Microscopy of Nanostructures*, ed by H. Hopster, H.P. Oepen, (Springer, Berlin Heidelberg New York 2004) pp 137–167
20. K. Koike, H. Hasegawa: Appl. Phys. Lett. **45**, 585 (1985)
21. H.P. Oepen, J. Kirschner: Phys. Rev. Lett. **62**, 819 (1989)
22. M.R. Scheinfein, J. Unguris, R.J. Celotta et al.: Phys. Rev. Lett. **63**, 668 (1989)
23. M. Konoto, T. Kohashi, K. Koike et al.: Phys. Rev. Lett. **93**, 107201 (2004)
24. J. Unguris, R.J. Celotta, D.T. Pierce: Phys. Rev. Lett. **69**, 1125 (1992)
25. M. Kleiber, M. Bode, R. Ravlić et al.: Phys. Rev. Lett. **85**, 4606 (2000)
26. U. Schlickum, N. Janke-Gilman, W. Wulfhekel et al.: Phys. Rev. Lett. **92**, 107203 (2004)
27. G. Steierl, G. Liu, D. Iorgov et al.: Rev. Sci. Instrum. **73**, 4264 (2002)
28. T. Duden, E. Bauer: Surf. Rev. Lett. **5**, 1213 (1998)
29. V.N. Strocov, H.I. Starnberg, P.O. Nilsson: Phys. Rev. B **56**, 1717 (1997)
30. E. Brüche: Z. Phys. **86**, 448 (1933)
31. W. Kuch, K. Fukumoto, J. Wang, C. Quitmann, F. Nolting, T. Ramsvik, unpublished result.
32. K.L. Man, M.S. Altman, H. Poppa: Surf. Sci. **480**, 163 (2001)
33. H. Poppa, E.D. Tober, A.K. Schmid: J. Appl. Phys. **91**, 6932 (2002).

34. J. Pohl: Zeitschr. f. techn. Physik **12**, 579 (1934)
35. H. Bethke, M. Klaua: Ultramicroscopy **11**, 207 (1983)
36. W. Engel, M.E. Kordesch, H.H. Rotermund et al.: Ultramicroscopy **36**, 148 (1991)
37. M.E. Kordesch, W. Engel, G.J. Lapeyre et al.: Appl. Phys. A **49**, 399 (1989)
38. M. Mundschau, M.E. Kordesch, B. Rausenberger et al.: Surf. Sci. **227**, 246 (1990)
39. H.H. Rotermund, S. Nettesheim, A. von Oertzen et al.: Surf. Sci. **275**, L645 (1992)
40. S. Nettesheim, A. von Oertzen, H.H. Rotermund et al.: J. Chem. Phys. **98**, 9977 (1993)
41. B.P. Tonner, G.R. Harp: Rev. Sci. Instrum. **59**, 853 (1988)
42. J. Stöhr, Y. Wu, M.G. Samant et al.: Science **259**, 658 (1993).
43. W. Swiech, G.H. Fecher, C. Ziethen et al.: J. Electron Spectrosc. Relat. Phenom. **84**, 171 (1997)
44. W. Kuch, R. Frömter, J. Gilles et al.: Surf. Rev. Lett. **5**, 1241 (1998)
45. S. Anders, H.A. Padmore, R.M. Duarte et al.: Rev. Sci. Instrum. **70**, 3973 (1999)
46. W. Kuch, J. Gilles, S.S. Kang et al.: Phys. Rev. B **62**, 3824 (2000)
47. L.I. Chelaru: Microscopic studies of interlayer magnetic coupling across nonmagnetic and antiferromagnetic spacer layers. PhD thesis, Martin-Luther-Universität Halle–Wittenberg, Halle (2003) (http://sundoc.bibliothek.uni-halle.de/diss-online/03/04H051)
48. W. Kuch, J. Gilles, X. Gao et al.: J. Magn. Magn. Mater. **242-245**, 1246 (2002)
49. W. Kuch, X. Gao, J. Kirschner: Phys. Rev. B **65**, 064406 (2002)
50. B.T. Thole, P. Carra, F. Sette et al.: Phys. Rev. Lett. **68**, 1943 (1992)
51. P. Carra, B.T. Thole, M. Altarelli et al.: Phys. Rev. Lett. **70**, 694 (1993)
52. W. Kuch: Imaging magnetic microspectroscopy. In: *Magnetic Microscopy of Nanostructures*, ed by H. Hopster, H.P. Oepen, (Springer, Berlin Heidelberg New York 2004) pp 1–28
53. W. Kuch, J. Gilles, F. Offi et al.: Surf. Sci. **480**, 153 (2001)
54. W. Kuch, L.I. Chelaru, K. Fukumoto et al.: Phys. Rev. B **67**, 214403 (2003)
55. D. Alders, L.H. Tjeng, F.C. Voogt et al.: Phys. Rev. B **57**, 11623 (1998)
56. S.S. Dhesi, G. van der Laan, E. Dudzik: Appl. Phys. Lett. **80**, 1613 (2002)
57. W. Kuch, L.I. Chelaru, F. Offi et al.: Phys. Rev. Lett. **92**, 017201 (2004)
58. W. Kuch, F. Offi, L.I. Chelaru, J. Wang, M. Kotsugi, and K. Fukumoto: unpublished result.
59. H. Ohldag, A. Scholl, F. Nolting et al.: Phys. Rev. Lett. **86**, 2878 (2001)
60. A. Scholl, J. Stöhr, J. Lüning et al.: Science **287**, 1014 (2000)
61. F. Nolting, A. Scholl, J. Stöhr et al.: Nature **405**, 767 (2000)
62. W. Kuch, L.I. Chelaru, F. Offi et al.: J. Vac. Sci. Technol. B **20**, 2543 (2002)
63. R. Nakajima, J. Stöhr, Y.U. Idzerda: Phys. Rev. B **59**, 6421 (1999)
64. G. Denbeaux, P. Fischer, G. Kusinski et al.: IEEE Trans. Magn. **37**, 2764 (2001)
65. P. Fischer, T. Eimüller, G. Schütz et al.: J. Appl. Phys. **89**, 7159 (2001)
66. P. Fischer, T. Eimüller, G. Schütz et al.: Rev. Sci. Instrum. **72**, 2322 (2001)
67. A. Thiaville, J. Miltat, J.M. García: Magnetic Force Microscopy: Images of Nanostructures and Contrast Modeling. In: *Magnetic Microscopy of Nanostructures*, ed by H. Hopster, H.P. Oepen, (Springer, Berlin Heidelberg New York 2004) pp 225–251

68. L. Abelmann, A. van den Bos, C. Lodder: Magnetic Force Microscopy – Towards Higher Resolution. In: *Magnetic Microscopy of Nanostructures*, ed by H. Hopster, H.P. Oepen, (Springer, Berlin Heidelberg New York 2004) pp 253–283
69. H.J. Hug, B. Stiefel, P.J.A. Van Schendel et al.: J. Appl. Phys. **83**, 5609 (1998)
70. J. Lohau, S. Kirsch, A. Carl et al.: J. Appl. Phys. **86**, 3410 (1999)
71. J. Lohau, S. Kirsch, A. Carl et al.: Appl. Phys. Lett. **76**, 3094 (2000)
72. P.J.A. Van Schendel, H.J. Hug, B. Stiefel et al.: J. Appl. Phys. **88**, 435 (2000)
73. M. Jullière: Phys. Lett. **54A**, 225 (1975)
74. M. Bode, M. Getzlaff, R. Wiesendanger: Phys. Rev. Lett. **81**, 4256 (1998)
75. A. Kubetzka, M. Bode, O. Pietzsch et al.: Phys. Rev. Lett. **88**, 057201 (2002)
76. W. Wulfhekel, J. Kirschner: Appl. Phys. Lett. **75**, 1944 (1999)
77. H.F. Ding, W. Wulfhekel, J. Kirschner: Europhys. Lett. **57**, 100 (2002)
78. U. Schlickum, W. Wulfhekel, J. Kirschner: Appl. Phys. Lett. **83**, 2016 (2003)
79. W.K. Hiebert, A. Stankiewicz, M.R. Freeman: Phys. Rev. Lett. **79**, 1134 (1997)
80. B.C. Choi, M. Belov, W.K. Hiebert et al.: Phys. Rev. Lett. **86**, 728 (2001)
81. A. Barman, V.V. Kruglyak, R.J. Hicken et al.: Appl. Phys. Lett. **82**, 3065 (2003)
82. J. Vogel, W. Kuch, M. Bonfim et al.: Appl. Phys. Lett. **82**, 2299 (2003)
83. A. Krasyuk, A. Oelsner, S.A. Nepijko et al.: App. Phys. A **76**, 863 (2003)
84. C.M. Schneider, A. Kuksov, A. Krasyuk et al.: Appl. Phys. Lett. **85**, 2562 (2004)
85. S.-B. Choe, Y. Acreman, A. Scholl et al.: Science **304**, 420 (2004)
86. H. Stoll, A. Puzic, B. van Waeyenberge et al.: Appl. Phys. Lett. **84**, 3328 (2004)
87. W. Kuch, J. Vogel, J. Camarero et al.: Appl. Phys. Lett. **85**, 440 (2004)
88. O. Scherzer, Optik **2**, 114 (1947)
89. H. Rose, Optik **85**, 19 (1990)
90. M. Haider, S. Uhlemann, E. Schwan et al.: Nature **392**, 768 (1998)
91. H. Rose, D. Preikszas: Nucl. Instrum. and Meth. A **363**, 301 (1995)
92. R. Fink, M.R. Weiss, E. Umbach et al.: J. Electron Spectrosc. Relat. Phenom. **84**, 231 (1997)
93. S. Eisebitt, M. Lörgen, W. Eberhardt et al.: Appl. Phys. Lett. **84**, 3373 (2004)
94. S. Eisebitt, J. Lüning, W.F. Schlotter et al.: Nature **432**, (2004)